POLITECNICO MILANO 1863

SCUOLA DI INGEGNERIA INDUSTRIALE E DELL'INFORMAZIONE

The effect of texture-induced motions on near-wall turbulence over super-hydrophobic surfaces

Tesi di Laurea Magistrale in
Aeronautical Engineering - Ingegneria Aeronautica

Raffaele Mancuso, 247497

Abstract: The data from a direct numerical simulation (DNS) of a turbulent channel flow over super-hydrophobic (SH) surfaces have been post-processed, in order to investigate the impact of this texture on the skin friction coefficient. The SH surface used in this work is composed by both longitudinal slip and no-slip stripes, which are alternated between each other along the spanwise direction. Super-hydrophobic surfaces generate a large decrease in drag because they allow the fluid close to the wall to slip along the streamwise and spanwise directions. In addition, the presence of the surface texture induces the formation of a texture-coherent flow that affects the near-wall turbulence. In particular, it is observed that, despite drag reduction is achieved, this coherent field increases the turbulent activity close to the wall, which has a negative effect on the amount of obtained drag reduction. The coherent motions have been separated from the stochastic one through a triple decomposition of both the velocity and pressure fields. Successively, in order to quantify the impact of this negative contribution, the triple decomposed FIK identity has been used. Furthermore, to understand the modifications induced in near-wall turbulence, the budget equations for Reynolds stresses have been used. In addition, by using the triple decomposition and the budget equations for Reynolds stresses, it has been possible to observe how the energy moves from the coherent field to the stochastic one and vice-versa. An important result that has been discovered using the mentioned tools reports that the formation of texture-induced motions decreases the magnitude of the achieved drag reduction by increasing the wall shear stress. Furthermore, it is discovered that this negative effect is induced by an energy flow close to the wall that goes from the stochastic field to the coherent one.

Advisor:
Prof. Alessandro Chiarini

Co-advisors:
Dr. Federica Gattere

Academic year:
2024-2025

Key-words: skin friction,triple decomposition,super-hydrophobic surfaces

1. Introduction

In turbulent channel flows there is a large variety of mechanisms that enable to reduce the value of the skin friction coefficient. This objective can be successfully achieved through the use of active and passive flow control techniques. In order to obtain drag reduction by means of an active mechanism, a power supply has to be provided. Some examples of active drag reduction techniques involve streamwise waves of spanwise velocity ([28]), pulsed jets used in the wake of bluff bodies ([3]), and reinforcement learning with partial measurements ([35]).

All these active techniques employ specific devices to induce a relaminarization of the flow close to the wall, decreasing the turbulent activity in this region. However, when the power involved in the generation of these oscillations is greater than the one saved, it is no more convenient to employ active flow control techniques. For this reason, passive drag reduction mechanisms have been investigated in the last decades.
The most widely used mechanism through which passive drag reduction is achieved involves specific types of surface roughness. Among all possible examples of surface roughness, riblets ([12]) and super-hydrophobic surfaces ([22]) have been object of research in the last years. However, SH surfaces enable to obtain high values of drag reduction by allowing the fluid to slip in some regions of the wall. This particular feature allows to decrease drag by values that can reach the 30% or more([14], [22]) with respect to the case in which SH surfaces are not used. Furthermore, super-hydrophobic surfaces are easier to model because they can be well modeled through the use of specific boundary conditions that represent the rough texture. This feature enables to maintain channel walls planarity, avoiding the introduction of problems related to roughness itself. However, the realization of hydrophobic surfaces represents a challenge from a technological point of view, and their ability to achieve high percentages of drag reduction has been object of investigation in the last decades.

Super-hydrophobic surfaces were introduced into the scientific community for the first time by Fakuda et al ([10]). A characteristic feature of this kind of surfaces is the presence of cavities, in which gas bubbles are trapped. Above these gas pockets, that are entrapped in between the roughness elements ([31]), the flow is free to slip across the streamwise and spanwise directions and, as a consequence, it is affected by an almost-zero shear stress. The gas pockets can be organized in posts or ridges, with the first ones affecting the homogeneity of both streamwise and spanwise directions, while the latter introduce heterogeneities only in the spanwise direction. In this thesis work, the features of only ridge-type surfaces are investigated because they represent the simplest case to deal with, which allows better focus on their effect on near-wall turbulence. In this work, the ridge-type surface is composed by longitudinal (aligned with the direction of the unperturbed flow) slip and no-slip stripes, which are alternated between each other along the spanwise direction.

1.1. State of the art: modeling of super-hydrophobic surfaces

From a computational point of view, in the most recent research activities ([7], [36]) SH surfaces have been modeled through the Navier slip condition ([24]), which imposes a partial slip condition. Through this condition, the value of the velocity field at the wall is proportional to its derivative, and the link between them resides in a quantity called "slip length". From a physical point of view, this parameter represents the distance perceived by the streamwise flow from an apparent, no-slip wall ([17]). An important contribution to the deeper understanding of the effects induced by this parameter on the skin friction coefficient has been made by Kim and Moin ([22]) and Fukagata et al. ([9]). In their work, they adopted the Reynolds decomposition to split the velocity field in a mean flow and a fluctuating part. After the application of this decomposition, they looked at the logarithmic mean velocity profile and at the root mean squares of the velocity fluctuations, discovering that drag reduction is obtained when imposing only a slip boundary condition for the streamwise velocity component. On the contrary, drag increase is observed when the same boundary condition is imposed only on the spanwise velocity component. The physical interpretation of these observed phenomena, provided by the authors, shows that drag reduction due to the streamwise slip is a direct consequence of the decrease in the wall shear stress, while the effect of the spanwise slip on the skin friction coefficient is indirect. In fact, a spanwise slip enhances the strength of near wall streamwise vortices, which results in a drag increase. By further observation, they discovered that when the slip boundary condition is imposed on both the streamwise and spanwise velocity components, a combination of the two previously discussed effects is reached. Based on the observations stated by Kim and Moin, Busse et al ([4]) demonstrated that, when a value above a certain threshold is assigned to the streamwise slip velocity, drag reduction is obtained regardless of the imposed spanwise slip velocity.

1.2. State of the art: Generation of secondary motions

In addition to these research activities, drag reduction obtained through super-hydrophobic surfaces is not the only interesting feature provided by this kind of roughness. In fact, inside of the channel, the presence of gas pockets separated from each other by equal distance towards the spanwise direction generates heterogeneities along this same direction. This loss of homogeneity creates secondary motions, which affect the turbulent activity near the walls. These secondary motions have been categorized by Prandtl ([27]) into three kinds. In particular, if a local spanwise inhomogeneity in wall conditions is present (e.g. surface roughness), secondary motions of Prandtl's second kind occur in plane or symmetrical wall-bounded flows. According to Stroh et al. ([34]), the presence of imperfections alters the homogeneity of Reynolds stresses in the spanwise direction, leading to the formation of this kind of secondary motions. In the work cited above, the authors discovered

that the roughness mean height has an impact on some Reynolds stresses components and, consequently, on the directionality of the secondary motions. In fact, if the mean streamwise velocity field is represented as a function of both the spanwise and the wall-normal coordinates, the roughness mean height is shown to affect the spanwise location of HMP (high momentum pathaways) and LMP (low momentum pathaways). The authors have observed that these modifications have an impact on some components of the Reynolds stresses and, as a consequence, on the direction of the secondary motions. The flow topology obtained close to the hydrophobic surfaces is similar to secondary flows over ridge-type roughness ([16]). As stated by Chung et al. ([5]), this kind of roughness induces secondary motions that generate HMP above the rough zones and LMP in the areas where slip conditions are imposed.
Neuhauser et al. ([25]) provided a physical explanation of the generation of these secondary motions induced by super-hydrophobic surfaces. To understand the formation of this texture-coherent flow, the authors studied the linear response of a laminar flow to infinitesimal perturbations. He observed that the different slip boundary conditions applied along the entire wall generate the deformation of spanwise perturbations added to the initial mean flow ([25]). This phenomenon occurs because the convection speed of the disturbance is higher in areas with the lowest shear stress. The loss of homogeneity in the spanwise direction causes the generation of further velocity components via continuity, yielding exponential growth of the disturbance. If a streamwise-average operator is applied to the flow during this growth phase, the velocity field features non-zero velocity components, compatible with secondary motions that are clearly visible as numerous couples of counter-rotating vortices.

1.3. State of the art: Effects induced by secondary motions

During the last decades, a lot of research activities have been centered on the effects induced by these secondary motions, and more in general of super-hydrophobic surfaces, on the near wall turbulent cycle. Hasegawa et al. ([14]) extended the FIK identity ([8]) to include all the components that contribute to skin friction in a turbulent channel flow with hydrophobic surfaces. The extended relation was further manipulated to obtain the dynamical contributions to the bulk mean velocity for hydrophobic surfaces. The final results of this research show that the mean bulk velocity is mainly affected by the effective slip length applied at the wall, while the turbulent contribution plays a less significant role.
Fairhall, Abderrahaman-Elena and Mayoral ([7]) investigated the effect that surface slip and surface texture have on turbulence over super-hydrophobic surfaces, using a triple decomposition of the flow. Through this filtering operation, the velocity field can be divided into a mean flow, a coherent field (which includes the flow induced by the spanwise pattern of the wall texture), and a fluctuating field. In their research, the authors show that drag reduction is proportional to the difference between the virtual origin perceived by the mean flow, and the one perceived by the overlying turbulence, as stated also by Luchini et al. ([20]). Furthermore, in this work, it is shown that not all triple decompositions are able to correctly separate the coherent field and the stochastic one, since the former appears to be modulated by the latter ([1], [2]).
Finally, Rastegari and Akhavan ([29]) computed Reynolds stresses and the terms of the budget equation for turbulent kinetic energy obtained with hydrophobic surfaces, in order to understand the link between drag reduction and the dimensions of the slip regions.

1.4. Objectives of this Thesis work

Taking into account all of these works, the objective of this thesis work is to understand how the secondary motions induced by super-hydrophobic surfaces affect the near-wall turbulence and, as a consequence, the drag at the wall. Specifically, the aim is to quantify the impact of the texture-coherent motions on the skin friction coefficient while focusing on the physical processes involved in this modification. The main steps followed to achieve these objectives involve the characterization of the flow field through the triple decoposition, as well as the FIK identity and budget equations for Reynolds stresses. In fact, as reported by Kawata and Tsukahara ([18]), budget equations for coherent and fluctuating stresses can be derived through triple decomposition. By analyzing previous literature, triple decomposed budget equations have never been applied to super-hydrophobic surfaces, and the change in drag induced by secondary motions have never been precisely quantified through the FIK identity. For this reason, the impact of SH surfaces on near-wall turbulence is seen from a completely different perspective compared to that found in the last research activities. In the following sections, details about the adopted computational resources and the governing equations are provided. In the Results section, the main features introduced by the surface texture on the flow field are presented, and the impact on drag of these phenomena is quantified. Finally, some details and explanations that justify the observed results are obtained using both the Reynolds decomposed and the triple decomposed budget equations for Reynolds stresses, which describe the governing physics behind the use of super-hydrophobic surfaces.

2. Methods

This section presents the procedure followed to understand the effect of SH surfaces on near-wall turbulence. First of all, some details about the database and the post-processing code are provided, and then the tools used to obtain the desired results are presented.

2.1. Database and Post-Processing code

The data from two DNS carried out in a fully developed turbulent channel flow, driven by constant pressure gradient (CPG), have been exploited in this work. The first simulation consists of $n_t = 50$ flow fields obtained in a classic channel flow without any kind of roughness distribution at the walls. The flow fields obtained from this simulation are used to validate the post-processing code that has been used to obtain the required results. In this work, the data obtained from this simulation will represent the "reference case". The second DNS, instead, involves 50 flow fields that have been carried out in a channel flow in which super-hydrophobic surfaces are located at the walls. For both the simulations, the time interval between every new field of the simulation is $\Delta t = 0.0056\frac{\delta}{u_\tau}$, where δ is the channel mean height and u_τ is the friction velocity. In addition, 35000 iterations occur between two consecutive saved fields. Consequently, every field is separated by 196 time units scaled with δ and u_τ. The adopted super-hydrophobic surfaces are composed by eight longitudinal slip stripes that are aligned with the flow direction. Furthermore, they are separated between each other by means of eight longitudinal no-slip stripes. For this reason, a total of $n_{sp} = 8$ texture periods are present in the spanwise direction. The DNS code, introduced by Luchini ([19]), solves the incompressible Navier–Stokes equations

$$\nabla \cdot \underline{u} = 0, \tag{1}$$

$$\frac{\partial \underline{u}}{\partial t} + \underline{u} \cdot \nabla \underline{u} = -\nabla p + \nu \nabla^2 \underline{u} \tag{2}$$

on a staggered Cartesian grid. The main feature of this grid lies in the adoption of four different grids to evaluate the three velocity components and the pressure, in order to avoid the born of spurious pressures due to the pressure gradient term in the Navier-Stokes equations. The momentum equations are advanced in time by a fractional time stepping method using a third-order Runge–Kutta scheme. The Poisson equation for the pressure is solved by an iterative successive over-relaxation (known as SOR) algorithm ([6]). Since every velocity component is computed on a different grid, during the post-processing the velocities have been interpolated to obtain quantities referred to the pressure grid. This procedure ensures that all the post-processed results are referred to the same grid. The streamwise, spanwise and wall-normal components of the velocity field will be called u, v and w respectively, while the streamwise, spanwise and wall-normal directions will be defined as x, y and z respectively. When the equations are written with the index notation, the components of the velocity field will be $u_1 = u$, $u_2 = v$ and $u_3 = w$, while the spatial directions will be $x_1 = x$, $x_2 = y$ and $x_3 = z$. Once these information have been provided, Figure 1 shows a sketch of the computational domain, as well as a single texture period. Each texture period is composed by a no-slip stripe (located at the center) and a slip stripe (which has been divided in two parts, located next to the no-slip region), and both stripes have the same length.

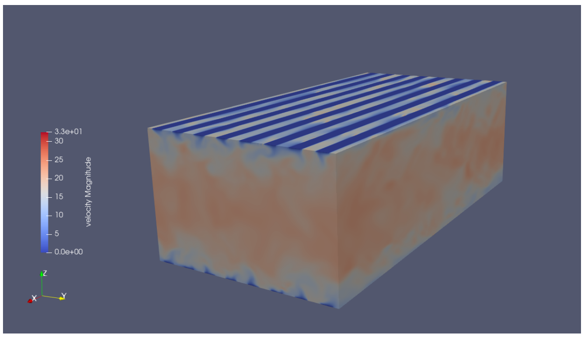

(a)

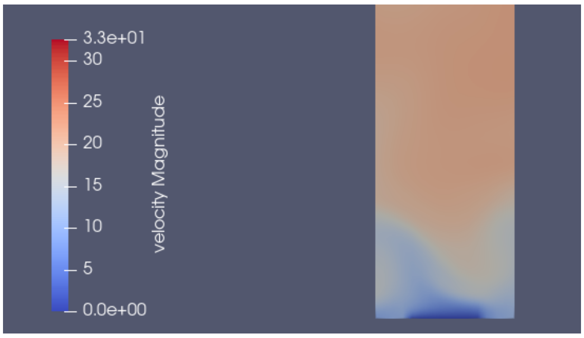

(b)

Figure 1: (a) sketch of the flow in a turbulent channel with SH surfaces; b) sketch of a texture period

The data from the simulations have been post-processed in order to compute the properties of the mean flow, the Reynolds stresses and other useful statistics. In order to perform the two DNS, periodic boundary conditions have been applied in both the streamwise and spanwise directions. Concerning the simulation carried out in the reference case, no-slip ($u = 0$,$v = 0$) and no-penetration ($w = 0$) boundary conditions have been imposed on both the lower wall and the upper one. For the simulations involving the usage of super-hydrophobic surfaces, instead, free slip ($\frac{\partial u}{\partial z} = 0$, $\frac{\partial v}{\partial z} = 0$) and no penetration boundary conditions have been imposed to simulate the presence of the wall texture. The numerical domain has a dimension of $(L_x \times L_y \times L_z) = (2\pi \times \pi \times 2\delta)$, and is discretized with $(n_x \times n_y \times n_z)$ grid points for both the simulations. For all DNS, the value of the friction Reynolds number $Re_\tau = \frac{u_\tau \delta}{\nu}$ has been fixed at 180, with $u_\tau = \sqrt{\frac{\tau_w}{\rho}}$, where τ_w and ρ are the wall shear stress and the fluid density, respectively. The quantities obtained from the simulations are adimensionalized on wall units. This procedure generates dimensionless data because the lengths are divided by δ_ν and the velocities are divided by u_τ. Every quantity expressed in wall units will be written with the superscript $.^+$. The simulation parameters for both the reference and the SH case are reported in Table 1. Furthermore, this Table displays also the bulk Reynolds number $Re_b = \frac{U_b \delta}{\nu}$.

	Re_b	Re_τ	n_x	n_y	n_z
Reference case	2850	180	128	128	130
SH case U_w^+	3300	180	128	128	130

Table 1: Simulation parameters

Looking at Table 1, it cab be observed that in the SH case Re_b is higher compared to the reference case. In CPG conditions, this features highlights drag reduction achieved in the SH case. In fact, in this situation drag is reduced by 25% compared to the reference case. A more precise derivation of this result will be provided in Section 3.

2.2. Triple decomposition of the flow-field

As stated in the previous section, a triple decomposition of the velocity field has been used in order to separate the secondary motions induced by the surface texture from the turbulent fluctuations. This decomposition was first introduced by Hussain and Reynolds ([15]), and starting from the Reynolds decomposition, it enables to write the velocity field $\underline{u}$ = u,v,w and the pressure field p as follows

$$\underline{u}(x, y, z, t) = \underline{U}(z) + \underline{u}'(x, y, z, t) = \underline{U}(z) + \underline{\widetilde{u}}(\widetilde{y}, z) + \underline{u}''(x, y, z, t), \tag{3}$$

$$p(x, y, z, t) = P(z) + \widetilde{p}(\widetilde{y}, z) + p''(x, y, z, t). \tag{4}$$

In Equation 3, the fluctuation with respect to the mean flow $\underline{u}'$ has been separated into two contributions. In fact, $\underline{U}(z)$, $\underline{\widetilde{u}}(\widetilde{y}, z)$ and $\underline{u}''(x, y, z, t)$ indicate the mean flow field, the coherent (or texture induced) field and the stochastic field, respectively. The definitions of all these components are reported below

$$\underline{U}(z) = \underline{\overline{u}}(z) = \frac{1}{n_x n_y n_t} \sum_{i=1}^{n_x} \sum_{j=1}^{n_y} \sum_{k=1}^{n_t} \underline{u}(x_i, y_j, z, t_k), \tag{5}$$

$$\underline{\widetilde{u}}(\widetilde{y}, z) = \frac{1}{n_x n_{sp} n_t} \sum_{i=1}^{n_x} \sum_{j=0}^{n_{sp}-1} \sum_{k=1}^{n_t} (\underline{u}(x_i, \widetilde{y} + j\frac{L_{ysp}}{L_y}, z, t_k) - \underline{U}(z)). \tag{6}$$

From Equation 5, it emerges that the mean flow field is obtained by averaging the instantaneous velocity fields in time, in the streamwise and in the spanwise directions. On the other hand, the coherent flow field is the result of an averaging of $\underline{u}'(x, y, z, t)$ in time, in the streamwise direction and in the number of periods (longitudinal strips) along the y direction. In fact, in Equation 6, n_{sp} represents the number of longitudinal strips in the channel, $\widetilde{y}$ denotes the local spanwise coordinate within the texture period and L_{ysp} is the length of this period. Through the use of Equations 3, 5 and 6 the velocity field contributions have been computed, and the sum of the mean flow and of the coherent field has been analyzed to capture some interesting physical details.
Using the triple decomposition, Reynolds stresses for hydrophobic surfaces can be written as follows

$$\langle u_i' u_j' \rangle = \langle (\widetilde{u}_i + u_i'')(\widetilde{u}_j + u_j'') \rangle = \langle \widetilde{u}_i \widetilde{u}_j \rangle + \langle \widetilde{u}_i u_j'' \rangle + \langle u_i'' \widetilde{u}_j \rangle + \langle u_i'' u_j'' \rangle, \tag{7}$$

where, the $\langle . \rangle$ operator denotes the average of the quantity . in time, in the x direction and in the number of texture periods n_{sp}. If the idempotency of the filter $\widetilde{.}$ is verified, then the cross stresses $\langle \widetilde{u}_i u_j'' \rangle$ and $\langle u_i'' \widetilde{u}_j \rangle$ are both zero, and the Reynolds stresses can be written as the sum of the coherent stresses ($\langle \widetilde{u}_i \widetilde{u}_j \rangle$) and the stochastic stresses ([1], [23]).

$$\langle u_i' u_j' \rangle = \langle \widetilde{u}_i \widetilde{u}_j \rangle + \langle u_i'' u_j'' \rangle. \tag{8}$$

By definition, the idempotency of a filter is verified if the application of the filter to an already filtered quantity does not change the result. For the purposes of this work, the idempotency is proved if

$$\widetilde{\widetilde{\underline{u}}}(\widetilde{y}, z) = \widetilde{\underline{u}}(\widetilde{y}, z). \tag{9}$$

It is possible to prove the relation reported in Equation 9 through the definitions of the $\widetilde{\cdot}$ operator (Equation 6) and of the $\underline{u}'$ field (Appendix B). In fact, according to Equation 3, it can be expressed as

$$\widetilde{\underline{u}}(\widetilde{y}, z) = \underline{u}(x, y, z, t) - \underline{U}(z) - \underline{u}''(x, y, z, t). \tag{10}$$

2.3. Drag computation through FIK identity

Once the intensity of the texture-coherent motions has been computed, the FIK identity ([8]) has been exploited in order to quantify the impact of these motions on drag. As previously, mentioned, Hasegawa et al. ([14]) manipulated the FIK identity in order to derive an expression for the bulk mean velocity U_b^+ ($U_b^+ = \frac{1}{L_z^+} \int_0^{2Re_\tau} U^+(z^+) dz^+$) obtained through super-hydrophobic surfaces. In this equation, the total bulk mean velocity is expressed as the sum of two terms: the mean streamwise slip velocity $U_w^+ = \overline{u}_w$ (which is the average of the streamwise velocities at the walls) and the relative bulk mean velocity

$$U_b^+ = U_w^+ + \frac{Re_\tau}{3} - \frac{1}{2} \int_0^{2Re_\tau} \frac{(z^+ - 1)}{Re_\tau} \langle u'^+ w'^+ \rangle \, dz^+. \tag{11}$$

Equation 11 denotes that the total bulk mean velocity is made up of three contributions: the one induced by the streamwise slip imposed at the wall, the one typical of the laminar flow, and the turbulent one. In particular, this last contribution can be seen as a weighted sum over the wall normal coordinates of the shear stress $\langle u'w' \rangle$. Through the use of Equation 11, the skin friction coefficient C_f can be computed recalling that, in the CPG case

$$C_f = \frac{2}{{U_b^+}^2}. \tag{12}$$

Equation 12 denotes that if the total bulk mean velocity is increased compared to the reference case, drag reduction is achieved, while if it decreases, the drag is increased.

2.4. Budget Equations for the Reynolds stresses

After the impact of SH surfaces on drag is quantified, budget equations for Reynolds stresses have been implemented to capture the difference introduced in the flow dynamics by the surface texture. The behaviour of the Reynolds stresses in a turbulent channel flow was investigated for the first time by Mansour et al. ([21]). In their research, the budget equations in index notation obtained by applying the classic Reynolds decomposition are reported as follows

$$\frac{\partial \langle u_i' u_j' \rangle}{\partial t} + U_k \frac{\partial \langle u_i' u_j' \rangle}{\partial x_k} = P_{ij} + T_{ij} + D_{ij} + Pr_{ij} + \varepsilon_{ij} + \Pi_{ij}. \tag{13}$$

The definition of each term in Equation 13 is reported below

$$P_{ij} = -\langle u_i' u_k' \rangle \frac{\partial U_j}{\partial x_k} - \langle u_j' u_k' \rangle \frac{\partial U_i}{\partial x_k}, \tag{14}$$

$$T_{ij} = -\frac{\partial \langle u_i' u_j' u_k' \rangle}{\partial x_k}, \tag{15}$$

$$D_{ij} = \nu \frac{\partial^2 \langle u_i' u_j' \rangle}{\partial x_k^2}, \tag{16}$$

$$Pr_{ij} = -\frac{\partial}{\partial x_k} (\delta_{jk} \frac{\langle u_i' p' \rangle}{\rho} + \delta_{ik} \frac{\langle u_j' p' \rangle}{\rho}), \tag{17}$$

$$\varepsilon_{ij} = -2\nu \langle \frac{\partial u_i'}{\partial x_k} \frac{\partial u_j'}{\partial x_k} \rangle, \tag{18}$$

$$\Pi_{ij} = \frac{1}{\rho} \langle p' \frac{\partial u_i'}{\partial x_j} + p' \frac{\partial u_j'}{\partial x_i} \rangle. \tag{19}$$

The physical explanation of each term reported in Equation 13 is now provided ([26]). P_{ij} is called Production rate, and explains how energy moves from the meanflow to the fluctuations or vice-versa, while ε_{ij} represents the dissipation rate. Π_{ij} is known as the pressure-strain term, and highlights how the energy moves from one component of the Reynolds stresses to another. In fact, the trace of Π_{ij} is zero, meaning that it is a redistributive term for the diagonal components of the Reynolds stress tensor. For the extra-diagonal terms, Π_{ij} can be either a source or a sink. In fact, these three terms are sources (or sinks) of energy, and whenever an imbalance between them occurs, the transport terms redistribute energy in the domain to satisfy the budget equations. T_{ij}, D_{ij} and Pr_{ij} denote the turbulent transport, the viscous diffusion and the pressure transport, respectively. Each term of the budget equations have been computed, starting from the DNS data, through the implementation of a centered finite difference scheme. Every term of Equation 13 is evaluated as a function of the wall-normal coordinate z, to allow an easier comparison with the reference case budget. Furthermore, the terms of the budget equations have also been computed as functions of both $\widetilde{y}$ and z. This procedure is followed in order to understand the effect of spanwise heterogeneities on the Reynolds stresses budget. Following [30], triple decomposition (Equation 3) can be applied to Equation 13, and this procedure enables to obtain distinct budgets for the coherent and stochastic stresses. The resulting equations, written in the case of a steady flowfield, are reported below

$$\begin{aligned}
&\underbrace{U_k \left\langle \frac{\partial}{\partial x_k} \widetilde{u}_i \widetilde{u}_j \right\rangle}_{\widetilde{M}_{ij}} \underbrace{+ \langle \widetilde{u}_i \widetilde{u}_k \rangle \frac{\partial U_j}{\partial x_k} + \langle \widetilde{u}_j \widetilde{u}_k \rangle \frac{\partial U_i}{\partial x_k}}_{\widetilde{P}_{ij}} \\
&\quad \underbrace{+ \frac{\partial}{\partial x_k} \langle \widetilde{u}_i \widetilde{u}_j \widetilde{u}_k \rangle + \frac{\partial}{\partial x_k} \langle \widetilde{u}_i \widetilde{u}_j u_k'' \rangle + \frac{\partial}{\partial x_k} \langle u_i'' \widetilde{u}_j u_k'' \rangle + \frac{\partial}{\partial x_k} \langle \widetilde{u}_i u_j'' u_k'' \rangle}_{\widetilde{T}_{ij}} \\
&\quad \underbrace{+ \left\langle \widetilde{u}_j \widetilde{u}_k \frac{\partial u_i''}{\partial x_k} \right\rangle + \left\langle \widetilde{u}_i \widetilde{u}_k \frac{\partial u_j''}{\partial x_k} \right\rangle}_{P_{cs,ij}} \underbrace{- \left\langle u_i'' u_k'' \frac{\partial \widetilde{u}_j}{\partial x_k} \right\rangle - \left\langle u_j'' u_k'' \frac{\partial \widetilde{u}_i}{\partial x_k} \right\rangle}_{P_{sc,ij}} \\
&= \underbrace{-\frac{1}{\rho} \langle \widetilde{p} (\widetilde{u}_i \delta_{jk} + \widetilde{u}_j \delta_{ik}) \rangle}_{\widetilde{Pr}_{ij}} \underbrace{+ \frac{1}{\rho} \langle \widetilde{p} (\frac{\partial \widetilde{u}_i}{\partial x_j} + \frac{\partial \widetilde{u}_j}{\partial x_i}) \rangle}_{\widetilde{\Pi}_{ij}} \underbrace{+ \nu \frac{\partial^2}{\partial x_k \partial x_k} \langle \widetilde{u}_i \widetilde{u}_j \rangle}_{\widetilde{D}_{ij}} \underbrace{- 2\nu \left\langle \frac{\partial \widetilde{u}_i}{\partial x_k} \frac{\partial \widetilde{u}_j}{\partial x_k} \right\rangle}_{\widetilde{\varepsilon}_{ij}},
\end{aligned} \tag{20}$$

$$
\begin{aligned}
&\underbrace{U_k \left\langle \frac{\partial}{\partial x_k} u_i'' u_j'' \right\rangle}_{M_{ij}''} \underbrace{+ \langle u_i'' u_k'' \rangle \frac{\partial U_j}{\partial x_k} + \langle u_j'' u_k'' \rangle \frac{\partial U_i}{\partial x_k}}_{P_{ij}''} \\
&\quad \underbrace{+ \frac{\partial}{\partial x_k} \langle u_i'' u_j'' u_k'' \rangle + \frac{\partial}{\partial x_k} \langle u_i'' u_j'' \widetilde{u}_k \rangle + \frac{\partial}{\partial x_k} \langle \widetilde{u}_i u_j'' \widetilde{u}_k \rangle + \frac{\partial}{\partial x_k} \langle u_i'' \widetilde{u}_j \widetilde{u}_k \rangle}_{T_{ij}''} \\
&\quad \underbrace{+ \left\langle u_j'' u_k'' \frac{\partial \widetilde{u}_i}{\partial x_k} \right\rangle + \left\langle u_i'' u_k'' \frac{\partial \widetilde{u}_j}{\partial x_k} \right\rangle}_{P_{sc,ij}} \underbrace{- \left\langle \widetilde{u}_i \widetilde{u}_k \frac{\partial u_j''}{\partial x_k} \right\rangle - \left\langle \widetilde{u}_j \widetilde{u}_k \frac{\partial u_i''}{\partial x_k} \right\rangle}_{P_{cs,ij}} \\
&= \underbrace{- \frac{1}{\rho} \langle p'' (u_i'' \delta_{jk} + u_j'' \delta_{ik}) \rangle}_{Pr_{ij}''} \underbrace{+ \frac{1}{\rho} \langle p'' (\frac{\partial u_i''}{\partial x_j} + \frac{\partial u_j''}{\partial x_i}) \rangle}_{\Pi_{ij}''} \underbrace{+ \nu \frac{\partial^2}{\partial x_k \partial x_k} \langle u_i'' u_j'' \rangle}_{D_{ij}''} \underbrace{- 2\nu \left\langle \frac{\partial u_i''}{\partial x_k} \frac{\partial u_j''}{\partial x_k} \right\rangle}_{\varepsilon_{ij}''} . \qquad (21)
\end{aligned}
$$

The last four terms on the left-hand side of Equation 20 are called interscale transport and they do not appear in Equation 13. In fact, they explain how energy moves from the secondary motions to the stochastic field and vice-versa. For this reason, they appear also in Equation 21, but with opposite signs compared to the ones shown in Equation 20. It is important to state that these equations are valid not only for SH surfaces, but for every kind of surface texture that induces a coherent flow.

3. Results

This section presents the main results obtained in this thesis work. First of all, the properties of the mean flow field and the Reynolds stresses close to the wall will be described. Successively, the FIK will be used to quantify the contributions of both the coherent field and the stochastic one on drag. After the computation of these impacts, the budget equations for Reynolds stresses with Reynolds decomposition will be used to explain the modifications induced by SH surfaces on the Reynolds stresses. Finally, the triple decomposed budget equations for Reynolds stresses will be employed to understand how the interaction between the stochastic field and the coherent one affects the observed changes in drag.

3.1. Characterization of the flowfield

3.1.1 Properties of the Mean Flow

Figure 2(a) shows the mean streamwise velocity profile in linear scale, while Figure 2(b) shows the same velocity profile in logarithmic scale, for both the reference case and the super-hydrophobic one. As seen in Figure 1(a), the use of surface texture generates a non-zero value of the streamwise slip velocity at the walls, as the fluid over the slip stripes (which mimick the presence of the gas pockets) is free to move in the x and y directions. Figure 2(b) represents that the logarithmic velocity profile obtained in the reference case is in good agreement compared to the "law of the wall" for turbulent channel flows, which states that

$$
\begin{aligned}
&U^+ \approx z^+, z^+ \leq 5, \\
&U^+ = \frac{1}{k} log(z^+) + B, z^+ > 30, \qquad (22)
\end{aligned}
$$

where $k \approx 0.4$ is the Von-Karman constant and $B \approx 5.2$. Furthermore, Figure 2(b) shows that super-hydrophobic surfaces induce an upward shift of the logarithmic profile obtained in the reference case. In fact, according to the classical theory of wall turbulence, the effect of small textures on the outer flow is a uniform shift in the mean velocity profile, compared to a smooth surface ([11]). When this displacement is directed upward, drag reduction is achieved, while drag increase is obtained when there is a downward shift. Furthermore, Figure 2(b) shows that the upward shift between the two logarithmic profile is not constant in the z direction. In fact, at the wall the shift is due to the slip boundary conditions imposed on the slip stripes, while moving toward the log region the upward shift becomes progressively smaller, reaching a value of $\Delta U^+ \approx 2.15$. This means that in the log region there is a negative behavior that affects drag reduction induced by the super-hydrophobic surface. Through this section, the creation of this negative effect is investigated. Furthermore, the mean streamwise slip velocity at the wall has a value of $U_w^+ \approx 6$, which represents an average between the high velocities over the slip stripes and the zero velocities over the no-slip stripes (Figure 1).

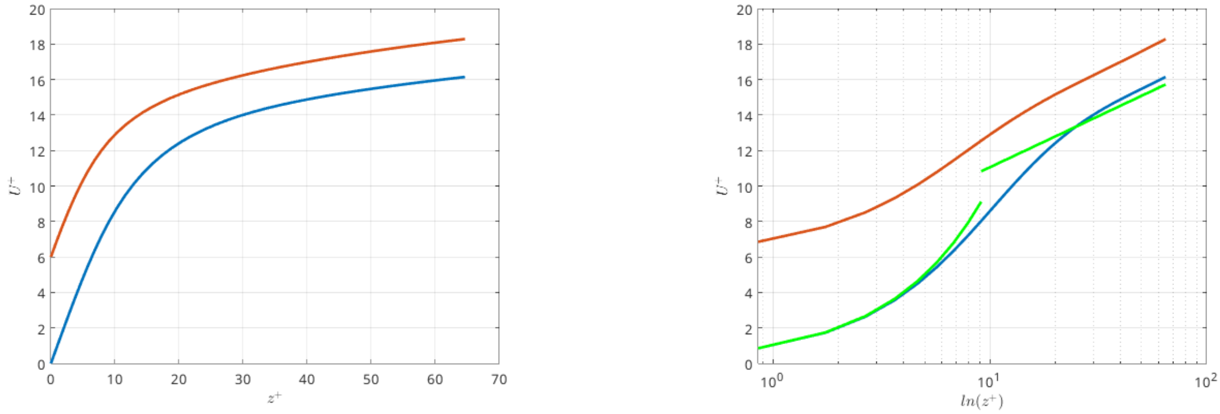

(a) (b)

Figure 2: Mean streamwise velocity profile in (a) linear scale and (b) logarithmic scale . Blue lines: reference case, orange line: SH case. Green line in b): law of the wall

In order to comprehend the contribution of secondary motions to drag reduction, is essential to introduce their main features. Figure 3(a) shows the sum of the mean streamwise velocity $\underline{U}(z)$ and the coherent streamwise velocity $\widetilde{\underline{u}}(y,z)$ on a texture period. It can be clearly seen that low momentum pathaways are located over the no-slip region, while high momentum pathaways can be found above the slip region. The occurrence of these phenomena can be explained by Figure 3(b), which shows the streamlines of the coherent field. The secondary motions, described as a pair of counter-rotating vortices, carry low-velocity fluid from the proximity of the no-slip region toward the bulk of the flow. In contrast, high-velocity fluid is carried by the clockwise vortices from the center of the channel toward the slip stripes.

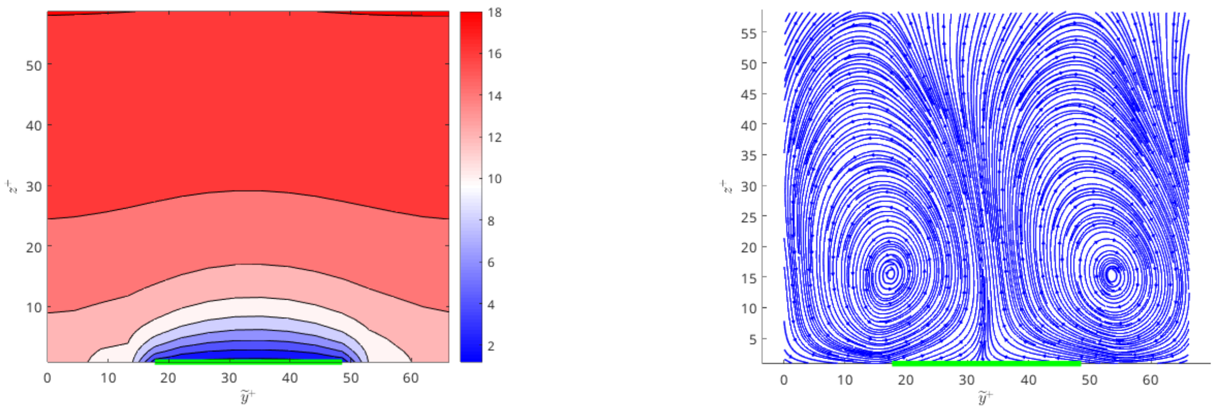

(a) (b)

Figure 3: (a) sum of the mean and coherent streamwise fields $U + \widetilde{u}$; (b) streamlines of the coherent field. Green lines: no-slip stripe

This distribution of HMP and LMP has already been observed by Stroh et al. ([34]), during their investigation of spanwise heterogeneous roughness. In particular, when wall roughness has a mean height equal to zero, the very same secondary motions induced by super-hydrophobic surfaces can be observed.

3.1.2 Second order statistics of the velocity field $\underline{u}'$

Once the main features of the mean flow have been reported, Reynolds stresses $\langle u_i' u_j' \rangle$ have been computed and validated using the data from Seo et al. ([33]). It will be seen that little discrepancies emerge from the comparison due to the different boundary conditions imposed at the wall. Furthermore, validation data are obtained for slip regions arranged in posts, where heterogeneities are also present in the streamwise direction. Figure 4 shows that the presence of texture-induced motions close to the wall has a direct impact on the Reynolds stresses profiles. In fact, the velocity fluctuations are very similar when compared with the reference case, with the exception of the near wall region. Here, the spanwise fluctuations experience an increase with respect to those obtained from the reference case. This is due to the secondary lateral motions and to their freedom to move at the $z^+ = 0$ plane ([32]). Also the wall-normal fluctuations, which at the boundary are very small for the slip stripes, are higher in the immediate proximity of the wall. This feature also affects the wall shear stress $\langle u'w' \rangle$ by increasing its values and shifting its peak toward the wall. Finally, the streamwise fluctuations obtained through hydrophobic surfaces present a peak located at the wall, which comes from the degree of freedom that enables the fluid to move along the streamwise direction.

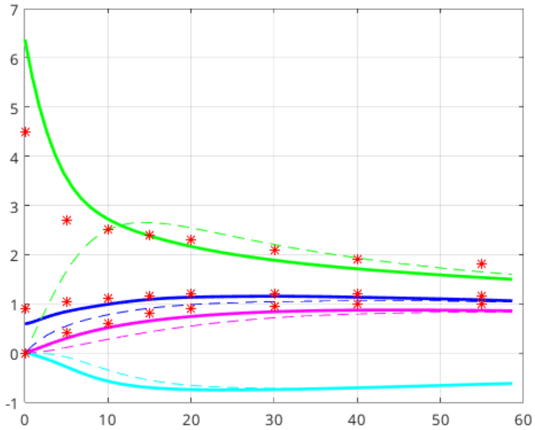

Figure 4: Comparison between turbulent fluctuations and wall shear stress obtained for both the reference case (dotted lines) and the slip/no-slip case (solid lines). Green: u'^+, Blue:v'^+, Purple: w'^+, Cyan: $\langle u'w' \rangle$. Red dots: data from Seo et al. ([33])

All these mentioned features of the Reynolds stresses profiles enable to conclude that the use of SH surfaces introduces higher anisotropies compared to those of the reference case. This phenomenon can be deduced because the difference between the rms of the velocity fluctuations at the wall is much higher compared to the reference case. This higher anisotropy is induced by the high derivatives in the spanwise direction introduced by the surface texture. Furthermore, this change in the spanwise derivatives can be observed by looking at Figures 5 and 6. In Figure 5, the terms of the budget equation for the turbulent kinetic energy are represented, for both the reference case and the super-hydrophobic one. All the contributions of this budget equation are obtained recalling that TKE is half of the trace of the diagonal components of the Reynolds stress tensor $(k' = \frac{1}{2}(\langle u'u' \rangle + \langle v'v' \rangle + \langle w'w' \rangle))$. For this reason, half of the trace of Equation 13 gives the budget equation for TKE.

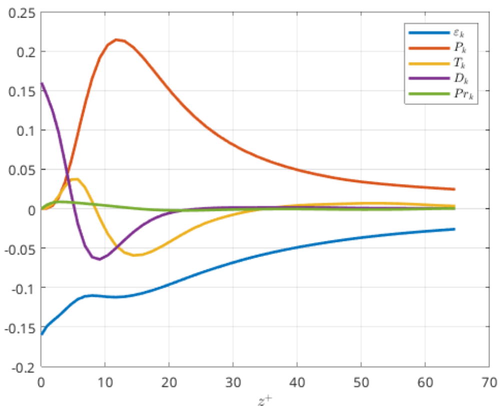

(a)

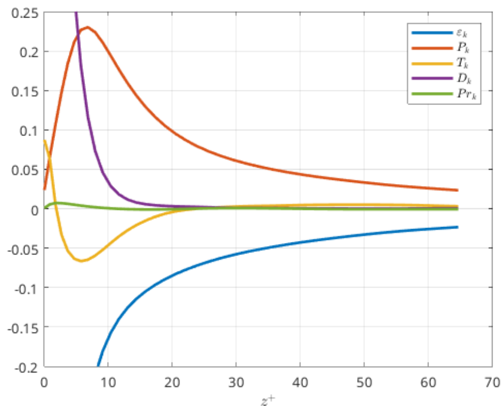

(b)

Figure 5: terms of the budget equation for k' in the a) reference case and b)SH surfaces cases

Figure 5 denotes that there are some important differences introduced by the surface texture, and the most important ones reside on the Pseudodissipation and viscous transport of k'. In fact, these two terms contain spatial derivatives of the second order and, consequently, the high gradients close to the wall in the spanwise direction have a significant impact on them. To obtain more details about the evolution in space of ε_k and

D_k, their plots over a texture period (and also the one of k') are reported in Figure 6. The turbulent kinetic energy has its maximum values above the low-shear regions, and the curvature of its isolines shows the effect of HMPs and LMPs induced by the secondary motions. It can be noticed that the peaks of Pseudodissipation are located at the interfaces between the high-shear region and the low-shear one. This happens because these interfaces are characterized by large values of the derivatives in the spanwise direction. Furthermore, at the wall the effect of Pseudodissipation is balanced by the viscous transport. In fact, also this transport component is characterized by high magnitudes at the interfaces between the slip and no-slip stripes. In conclusion, the high derivatives between the stripes greatly affect the budget equation for k' in the SH case.

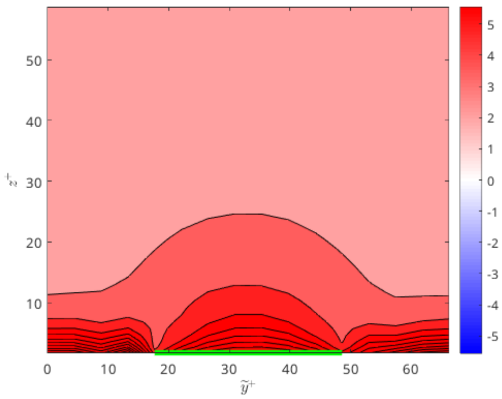

(a) k'

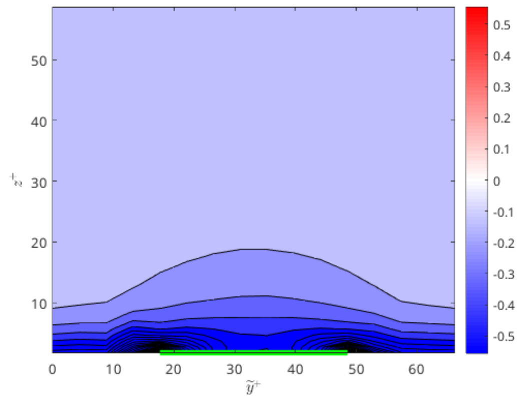

(b) ε_k

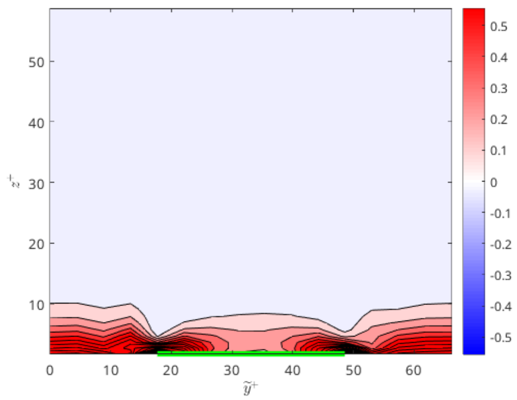

(c) D_k

Figure 6: Turbulent kinetic energy, Pseudodissipation and Viscous Transport over a texture period in the SH case. Green lines: no-slip stripe

3.1.3 Application of the triple decomposition to the Reynolds stresses

As stated in Section 1, secondary motions of Prandtl's second kind occur when a spanwise variation of the Reynolds stresses is present. For this reason, it is useful to represent these stresses as functions of y^+ and z^+. In particular, secondary motions can be clearly observed looking at the wall shear stress $\langle v'w' \rangle$, as shown in Figure 7. The shape of this stress is in good agreement with the results reported in Stroh et al. ([34]) obtained for ridge-type roughness. Furthermore, it is crucial to represent this Reynolds stress in two dimensions because of its anti-symmetric behavior with respect to the center of the texture period. In fact, when an average in the spanwise direction is performed, $\langle v'w' \rangle$ is not visible because it cancels out.

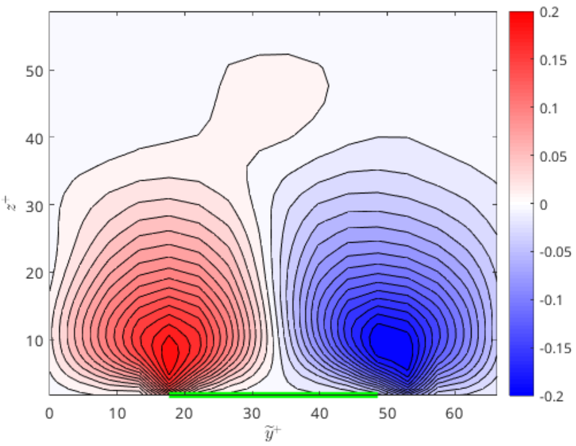

Figure 7: Reynolds stress $\langle v'w' \rangle$ obtained through the use of super-hydrophobic surfaces. Green line: no-slip stripe

In Figure 7, the peaks in the correlation between v' and w' are located at the interfaces between the no-slip and the slip regions, since high spanwise velocity fluctuations can be found in these zones. The use of a triple decomposition of the velocity field enables to separate the dispersive (or coherent) stress $\langle \widetilde{v}\widetilde{w} \rangle$ from the stochastic one $\langle v''w'' \rangle$ in order to quantify their magnitude. Figure 8 represents the results obtained from the use of this decomposition, showing that the coherent stresses are much weaker than the stochastic ones. The explanation behind this phenomenon is given by Figure 9, which shows the values of $\widetilde{v}$ and $\widetilde{w}$ in a texture period. By analyzing this Figure, it emerges that the peaks of $\widetilde{v}$ are located at the interfaces between the high-shear zone and the low shear one. On the contrary, the peaks of $\widetilde{w}$ are located where HMPs and LMPs are induced by secondary motions. This space shift between the regions where the velocity components have their own maximum value leads to a loss of correlation between them and, consequently, to a low value of the shear stress $\langle \widetilde{v}\widetilde{w} \rangle$.

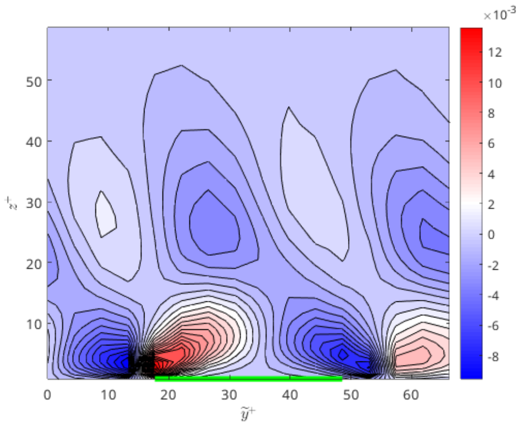

(a)

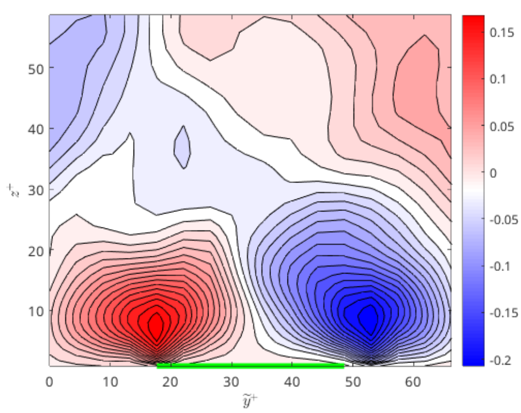

(b)

Figure 8: (a) coherent stresses $\langle \widetilde{v}\widetilde{w} \rangle$; (b) stochastic stresses $\langle v''w'' \rangle$. Green lines: no-slip stripe

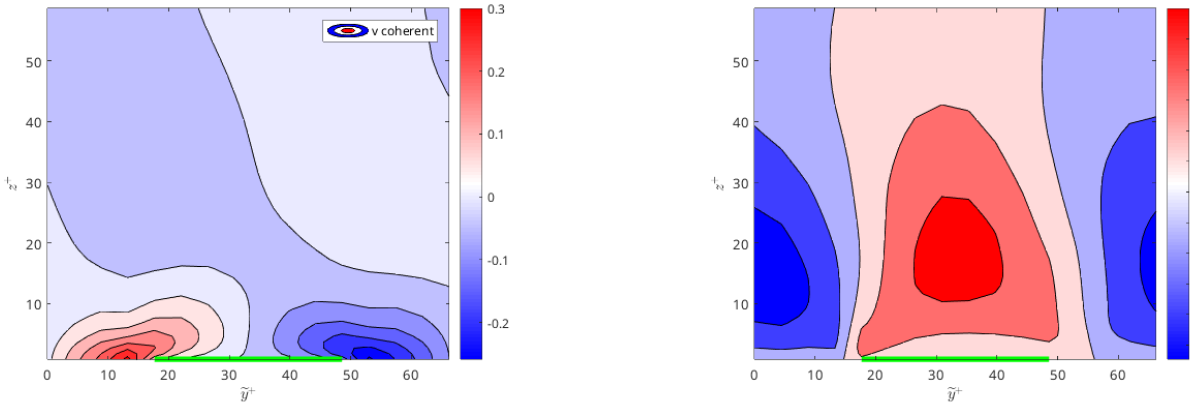

(a)

(b)

Figure 9: (a) phase-averaged spanwise velocity $\widetilde{v}$; (b) phase averaged wall normal velocity $\widetilde{w}$. Green lines: no-slip stripe

As previously stated in this section, the increase in the wall shear stress $\langle u'w' \rangle$ is due to the presence of secondary motions that have been visualized through Figures 8 and 9. In order to filter the contribution of these texture induced motion from the the total shear stress, the triple decomposition have been used. The magnitude of the obtained coherent and stochastic shear stresses ($\langle \widetilde{u}\widetilde{w} \rangle$ and $\langle u''w'' \rangle$) is shown in Figure 10 as a function of z^+.

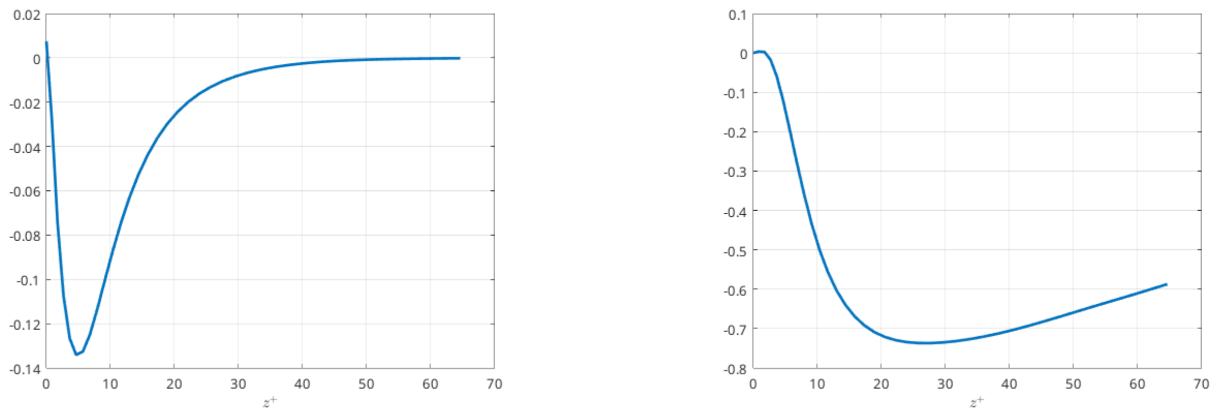

(a)

(b)

Figure 10: (a) dispersive wall shear stress $\langle \widetilde{u}\widetilde{w} \rangle$ and b) fluctuating wall shear stress $\langle u''w'' \rangle$

The coherent stress is very high near the wall since the effect of the texture is limited to the region $z^+ < 22$. In this section, drag reduction obtained by using SH surfaces has been observed, as well as the effect of secondary motions on the flow field close to the wall. Furthermore, it has been reported that, despite the drag reduction achievement, these motions increase the intensity of the total shear stress $\langle u'w' \rangle$.

3.2. Impact of the secondary motions on drag

Once the effect of secondary motions on the wall shear stress have been characterized, their impact on drag is now discussed. To perform this operation, the triple decomposed FIK identity has been used in order to link $\langle \widetilde{u}\widetilde{w} \rangle$ with U_b^+, which is directly related to the skin friction coefficient through Equation 12. If the triple decomposition is applied to the Reynolds stresses components, Equation 11 can be written as follows

$$U_b^+ = U_w^+ + \frac{Re_\tau}{3} - \left(\frac{1}{2}\int_{-Re_\tau}^{Re_\tau} \frac{z}{Re_\tau} \langle \widetilde{u}^+\widetilde{w}^+ \rangle \, dz + \frac{1}{2}\int_{-Re_\tau}^{Re_\tau} \frac{z}{Re_\tau} \langle u''^+w''^+ \rangle \, dz\right). \tag{23}$$

Table 2 shows the different contributions that appear in Equation 23, for both the SH and the reference case. In the FIK identity of the reference case ([8]), only the laminar and the turbulent contributions are present, while in the SH case also appears the effect of the slip velocity at the wall. Since Re_τ does not change for the reference and the SH case, the laminar contribution does not change as well. On the other hand, the turbulent contribution in the SH case is different from the reference case one because of the presence of texture-induced motions that affect the budget equations. With drag reduction techniques different from SH surfaces, the boundary conditions and the effect induced by roughness cause a decrease of the turbulent contribution and, for this reason, drag reduction is obtained. In contrast, for the SH case, the turbulent contribution is higher compared to the one computed in the reference case, and the higher value of U_b^+ is achieved through U_w^+.

	reference case (ref)	SH case
(1) U_b^+	15.8317	18.3757
(2) U_w^+	0	5.968
(3) $Re_\tau/3$	60	60
(4) $-\frac{1}{2}\int z^+\langle\tilde{u}\tilde{w}\rangle dz^+$	0	-1.733
(5) $-\frac{1}{2}\int z^+\langle u''w''\rangle dz^+$	-44.007	-45.817
(2)+(3)+(4)+(5)	15.99	18.41

Table 2: Contributions to the FIK identity

By looking at the values of the bulk mean velocity U_b^+ reported in Table 2, the skin friction coefficients in both the reference and SH case can be computed

$$C_{f,ref} = \frac{2}{{U_{b,ref}^+}^2} = 0,008,$$

$$C_{f,SH} = \frac{2}{{U_{b,SH}^+}^2} = 0,006.$$

From the knowledge of the skin friction coefficient, it is possible to compute the drag reduction percentage $\Delta C_{f,\%}$ as follows

$$\Delta C_{f,\%} = -\frac{C_{f,ref} - C_{f,SH}}{C_{f,ref}} \times 100 = -25\%.$$

Finally, the displacement of the logarithmic mean velocity profile ΔU^+ can be obtained through the following relation ([7])

$$DR = -\frac{\Delta C_f}{C_{f,ref}} = 1 - \frac{1}{(1 + \Delta U^+/U_{b,ref}^+)^2}. \tag{24}$$

By manipulating Equation 24, the value of ΔU^+ is obtained

$$\Delta U^+ \approx 2,4,$$

and it is very similar to the value reported in Section 3.1.1. In this section, the results provided in Sections 2.1 and 3.1.1 have been proved. Furthermore, it has been proved that secondary motions have a negative impact on the amount of achievable drag reduction.

3.3. 1D Budget equations for $\langle u_i'u_j'\rangle$

In order to provide an explanation for the increase in Reynolds shear stress $\langle u'w'\rangle$, which is directly related to the increase in drag due to near-wall turbulence, budget equations for Reynolds stresses are used. In particular, the budget equation for $\langle u'w'\rangle$ is carefully analyzed to understand which are the most relevant differences with respect to the reference case. Figure 11 shows the dominant terms in the budget equation for $\langle u'w'\rangle$, for both the reference case and the super-hydrophobic one. Since this shear stress is negative along all the z^+ coordinates (Figure 4), the terms in Figure 11 are negative when $\langle u'w'\rangle$ is produced and positive when it is dissipated.

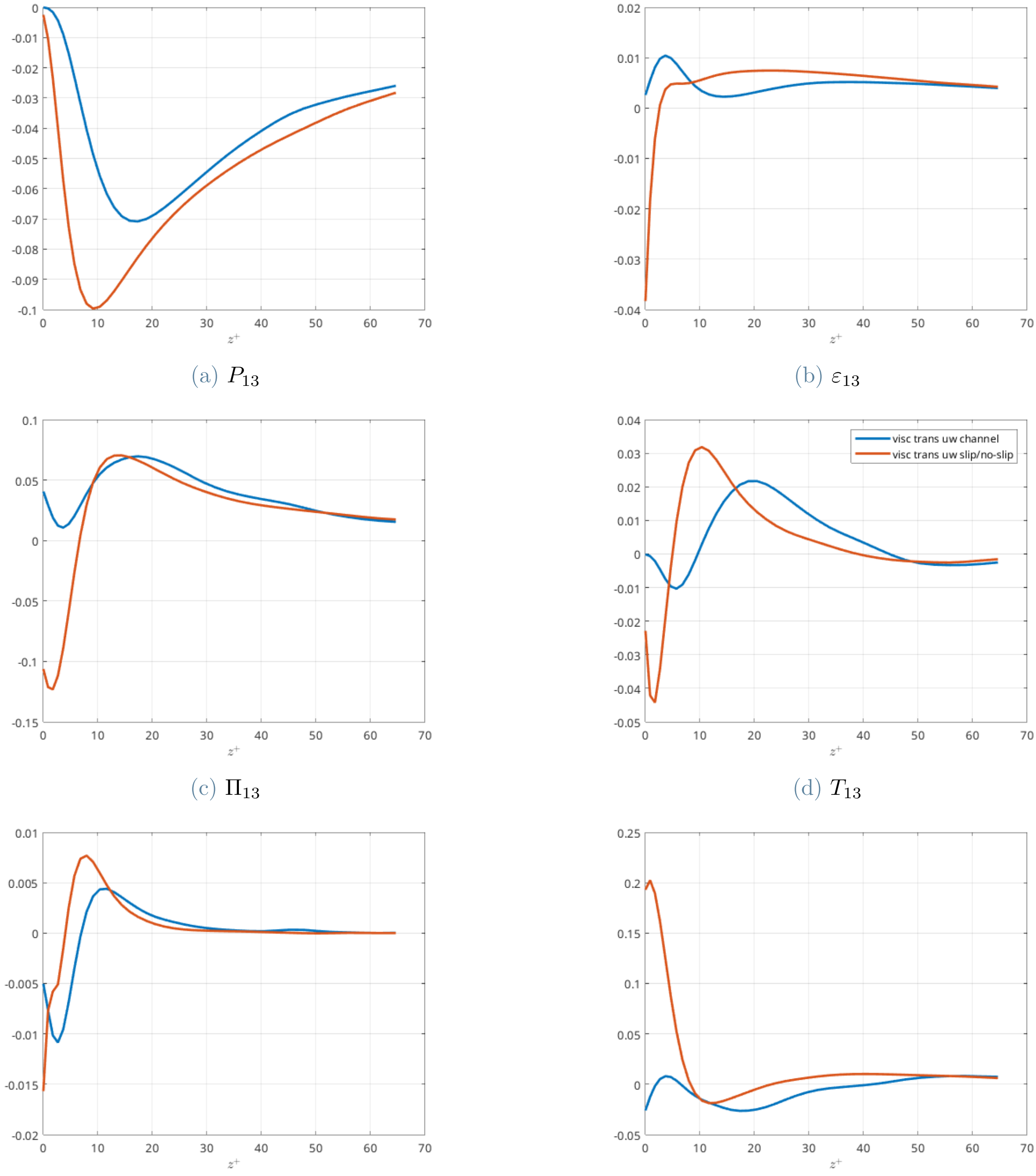

(a) P_{13} (b) ε_{13}

(c) Π_{13} (d) T_{13}

(e) D_{13} (f) Pr_{13}

Figure 11: Terms of the budget equation for $\langle u'w' \rangle$. Blue lines: reference case, orange lines: SH case

An interesting feature introduced by SH surfaces involves the production of $-\langle u'w' \rangle$, which is higher compared to the reference case. Furthermore, its maximum value is moved from $z^+ \approx 16$ to $z^+ \approx 10$, highlighting a shift toward the wall of approximately 6 wall units ($= U_w^+$). This phenomenon is interesting because it is in contrast with other drag reduction mechanisms, where the maximum value of the Reynolds stresses (and consequently of the production terms) is moved away from the wall ([13],[23]). The increase in the value of P_{13} can be explained by looking at Figure 12 and recalling that

$$P_{13} = -\langle w'w' \rangle \frac{\partial}{\partial z} U - \langle u'w' \rangle \frac{\partial}{\partial z} W \approx -\langle w'w' \rangle \frac{\partial}{\partial z} U. \tag{25}$$

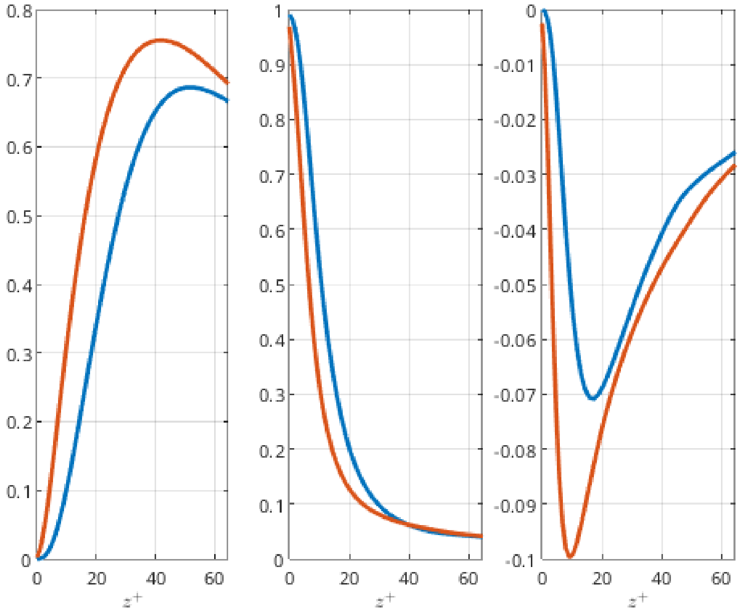

Figure 12: contributions to P_{13} for the reference case (blue line) and the SH one (orange line). From left to right: $\langle w'w'\rangle^+$, $\frac{\partial U^+}{\partial z^+}$ and P_{13}

Despite the reduction in $\frac{\partial U}{\partial z}$ introduced by the slip condition imposed on the streamwise velocity at the wall, the Reynolds stress $\langle w'w'\rangle$ is much higher when SH surfaces are used, and its peak is moved toward the wall. For this reasons, the Production of $\langle u'w'\rangle$ is higher compared to the reference case. The pressure strains term is smaller than the one obtained from the smooth-wall data for all the z^+ coordinates, and is very intense and negative at the wall. This behavior of pressure strains shows that they contribute to the increase in wall shear stress close to the wall. Another interesting difference between the reference case and the SH one resides in the Pseudodissipation term. In fact, the shape of this term is significantly modified by the presence of the surface texture, and it will be interesting to understand the main causes of this difference

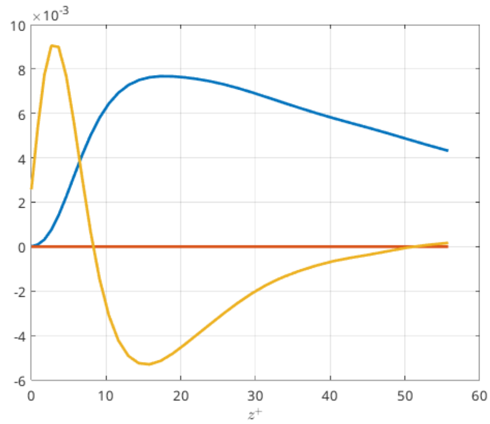

(a)

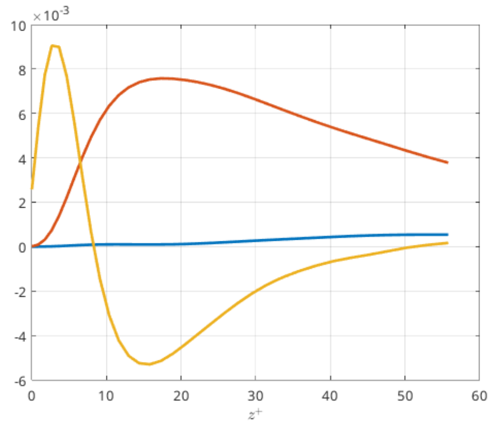

(b)

Figure 13: different contributions to ε_{13} for a) smooth wall case and b) SH case. blue line: $-2\nu\langle\frac{\partial u'}{\partial x}\frac{\partial w'}{\partial x}\rangle$, red line: $-2\nu\langle\frac{\partial u'}{\partial y}\frac{\partial w'}{\partial y}\rangle$, yellow line $-2\nu\langle\frac{\partial u'}{\partial z}\frac{\partial w'}{\partial z}\rangle$

Figure 13 displays the three contributions to ε_{13} (Equation 13), and it can be observed that the derivatives with respect to z^+ are the most significant near the wall. Instead, the positive peak of Pseudodissipation located at $z^+ \approx 22$ is due to the derivatives in the spanwise direction, which high values in this region are induced by the secondary motions (3). From these considerations, it can be deduced that SH surfaces can change significantly not only the magnitude but also the shape of some terms of the budget equations. Looking at the transport terms, they seem to be shifted toward the wall, while their shape is approximately unchanged if it is compared to the reference case. However, the intensity of the pressure transport changes drastically near the wall. In fact, in this region the pressure transport becomes positive, which means that it moves energy from the wall toward the bulk of the flow. This sudden increase in pressure transport obtained by using SH surfaces can be explained by recalling that

$$Pr_{13} = -\frac{1}{\rho}\frac{\partial}{\partial z}\langle p'u'\rangle. \tag{26}$$

Since SH surfaces are characterized by high values of streamwise velocity at the wall, the intensity of the pressure transport increases compared to that in the reference case. Finally, the viscous and turbulent transport moves energy from the buffer layer (approximately $8 < z^+ < 16$ for the SH case) to the inner and outer layer, accomplishing the same role of their reference case counterparts ([26]). Despite the differences in the intensities assumed by the transport terms in the region close to the wall ($z^+ < 16$), the increase in P_{13} represents the main factor that leads to an increase of $\langle u'w'\rangle$ in the region $z^+ < 20$.
As shown in Eq. 25, Reynolds stress $\langle w'w'\rangle$ greatly affects P_{13}, and for this reason, the evolution in space of $\langle w'w'\rangle$ is investigated by looking at its budget equation, which contributions are reported in Figure 14.

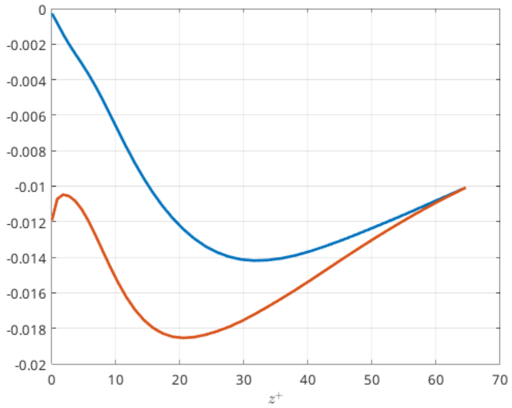

(a) ε_{33}

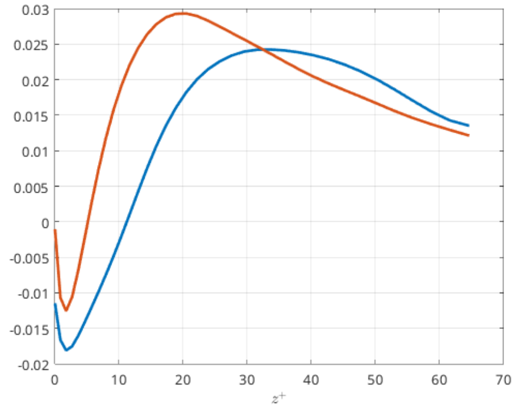

(b) Π_{33}

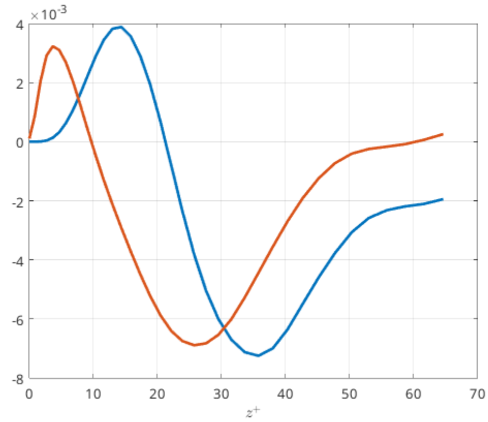

(c) T_{33}

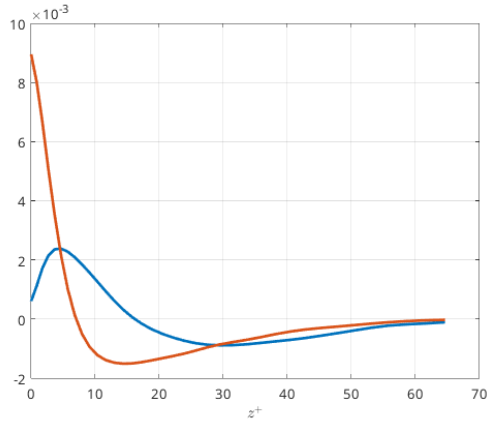

(d) D_{33}

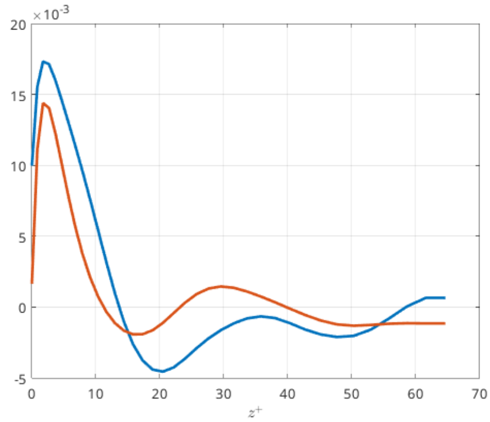

(e) Pr_{33}

Figure 14: Terms of the budget equation for $\langle w'w' \rangle$. Blue lines: reference case, orange lines: SH case

Looking at this Figure, it emerges that the pressure strain term Π_{33} is much higher when SH surfaces are used. The reason behind this behavior of the pressure strains can be found in recalling their redistributive properties. In fact, since the continuity equation must be respected, the diagonal components of the pressure strain tensor must satisfy the following relation

$$\Pi_{11} + \Pi_{22} + \Pi_{33} = 0. \tag{27}$$

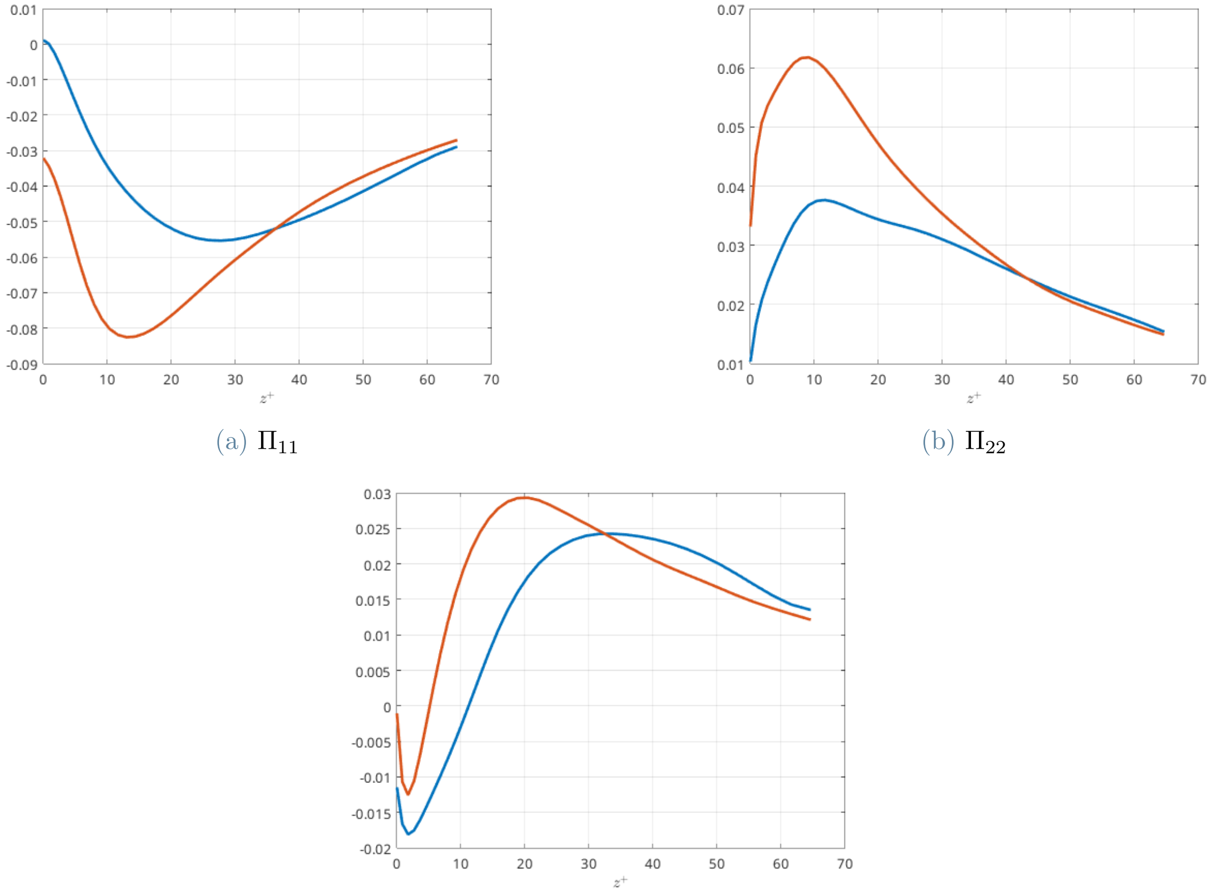

(a) Π_{11}

(b) Π_{22}

(c) Π_{33}

Figure 15: Diagonal component of the pressure strain tensor for the reference case (blue lines) and the SH one (orange line)

Figure 15 shows the diagonal components of the pressure strain tensor as functions of z^+. As can be seen, Π_{11} is always negative, which means that energy moves from $\langle u'u' \rangle$ to $\langle v'v' \rangle$ and $\langle w'w' \rangle$ along all the z^+ coordinates. Furthermore, from Equation 27, $\Pi_{22}/\Pi_{11} + \Pi_{33}/\Pi_{11} = -1$, which means that when the energy is evenly distributed among $\langle v'v' \rangle$ and $\langle w'w' \rangle$, $\Pi_{22}/\Pi_{11} = -0.5$ and $\Pi_{33}/\Pi_{11} = -0.5$. From Figure 15, it can be seen that both Π_{11} and Π_{22} exhibit some differences with respect to the reference case. In particular, the strong anisotropies of u' and v' (Figure 4) located at the wall change the redistribution of energy between the diagonal components of the Reynolds stresses. This feature introduced by SH surfaces can be explained through Figure 16, which shows how energy moves from $\langle u'u' \rangle$ to $\langle v'v' \rangle$ and $\langle w'w' \rangle$.

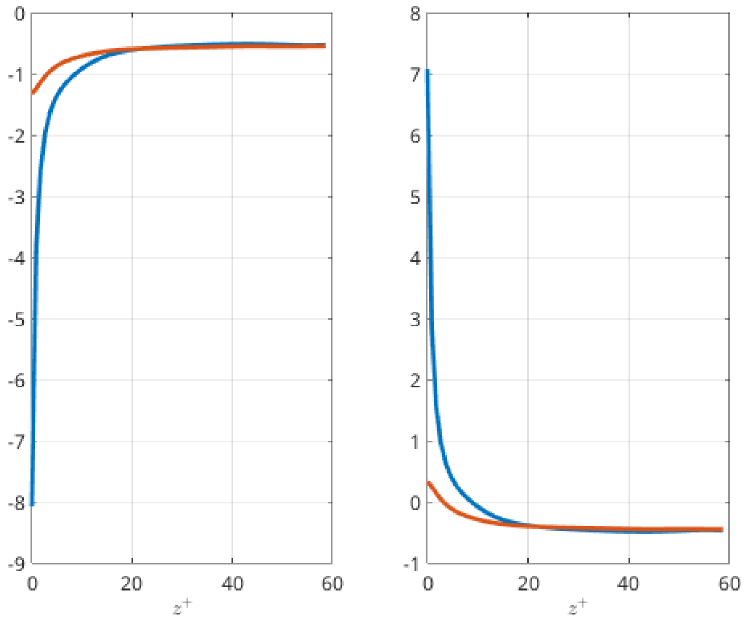

Figure 16: left: Π_{22}/Π_{11} for both the reference case (blue line) and the SH one (orange line); right: Π_{33}/Π_{11} for both the smooth wall case (blue line) and the SH one (orange line)

It can be noticed that $\langle w'w' \rangle$ loses less energy close to the wall compared to the smooth-wall case, while $\langle v'v' \rangle$ acquires less energy. In fact, since SH surfaces introduce a higher anisotropy of v' fluctuations, there is no need to redistribute energy to this velocity component. As a consequence, $\langle w'w' \rangle$ has an higher energy content due to this pressure strain behavior. The Pseudodissipation of this Reynolds stress is a more dissipative term compared to the reference case, and the transport terms appear to be shifted toward the wall without significant changes in their shape or intensity. As a consequence, also in this case the transport terms move energy from the buffer layer to the inner and outer flows ([26]). In general, it can be concluded that the action of the consuming term is not sufficient to balance the increase in the pressure strain term, which is the main responsible for the increase in $\langle w'w' \rangle$ in the region $z^+ < 20$.
In conclusion, Π_{33} has been shown to be the main factor that contributes to the increase in P_{13}, which is related to the increase in $\langle u'w' \rangle$ in the proximity of the texture

3.4. 1D Budget equations for $\langle \widetilde{u}_i \widetilde{u}_j \rangle$ and $\langle u''_i u''_j \rangle$

Using budget equations for Reynolds stresses, an explanation of the increase in $\langle u'w' \rangle$ has been provided. However, as previously said in Section 3.1.3, the coherent wall shear stress is the main factor $\langle \widetilde{u}\widetilde{w} \rangle$ that leads to an increase in the turbulent contribution of the FIK identity. For this reason, it is interesting to understand the interaction between the flow field induced by the secondary motions and the near-wall turbulence. To reach this purpose, Equations 20 and 21 are used, and their terms have been computed as functions of z^+ through an average over the texture period. However, the same terms have also been computed avoiding this average process, in order to obtain information about what happens in a texture period. Figure 17 shows the contributions of the budget equations for both the coherent and stochastic terms of $\langle u'w' \rangle$, as well as the terms of the budget equation for this shear stress in the reference case. In this Figure, the term $T''_{tot,13}$ and $\widetilde{T}_{tot,13}$ represent the sum of the stochastic and coherent transport terms, respectively. Both these terms have been represented to avoid the superimposition of too many terms of the budget equations.

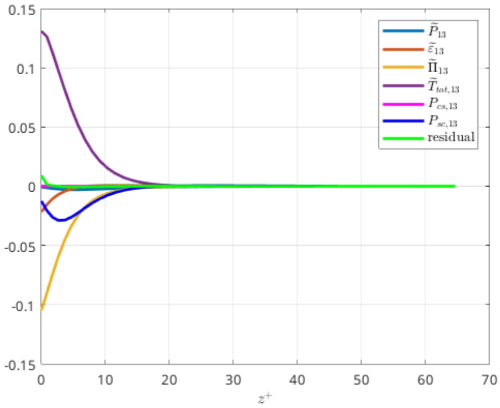

(a)

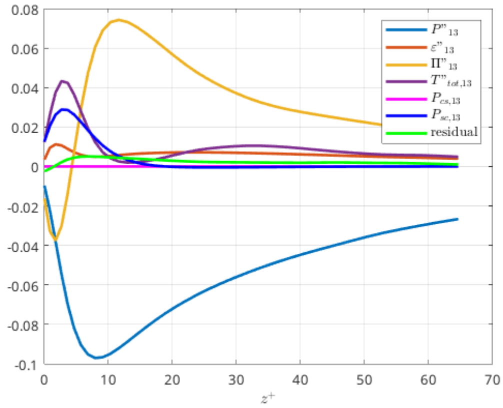

(b)

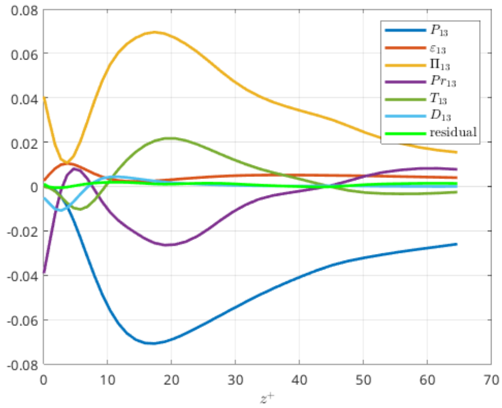

(c)

Figure 17: different terms of the budget equations for a) $\langle \widetilde{u}\widetilde{w} \rangle$, b) $\langle u''w'' \rangle$, c) $\langle u'w' \rangle$ in the reference case

It can be noticed that there are some differences between the fluctuating budgets obtained for both the reference and the super-hydrophobic case. P''_{13} is more intense than P'_{13}, and its peak is shifted toward the wall, meaning that the rough surface induces a larger amount of $-\langle u'w' \rangle$ in the near-wall region. However, the most interesting feature of the SH case is the presence of $P_{sc,13}$, which tells how energy is moved from the coherent field to the stochastic one. In particular, Figure 17(b) shows that this term is a dissipative one, and helps to close the balance at the wall carrying the energy that comes from the higher Production in Figure 17(b) from the stochastic field to the coherent one. Furthermore, looking at both P''_{13} and $P_{sc,13}$, it can be deduced that close to the wall energy is transferred from the mean flow to the stochastic one, and then from this field to the coherent one. For this reason, this energy flow induces the observed increase in shear stress $\langle \widetilde{u}\widetilde{w} \rangle$, which is the main factor that causes an increase in drag.

3.5. 2D Budget equations for $\langle \widetilde{u}_i \widetilde{u}_j \rangle$ and $\langle u''_i u''_j \rangle$

As reported in Section 2.1, SH surfaces are characterized by the presence of a spatial pattern in the spanwise direction. For this reason, interesting phenomena can be observed by looking at the budget equations for both the coherent and the stochastic stresses in two dimensions. The computed quantities are represented on a texture period, along the coordinates $\widetilde{y} - z$. Figure 18 represents the most important terms of the budget equations for $\langle u''w'' \rangle$ on a texture period. Furthermore, Figure 19 shows the distribution in a texture period of the most important terms of the budget equation for $\langle \widetilde{u}\widetilde{w} \rangle$.

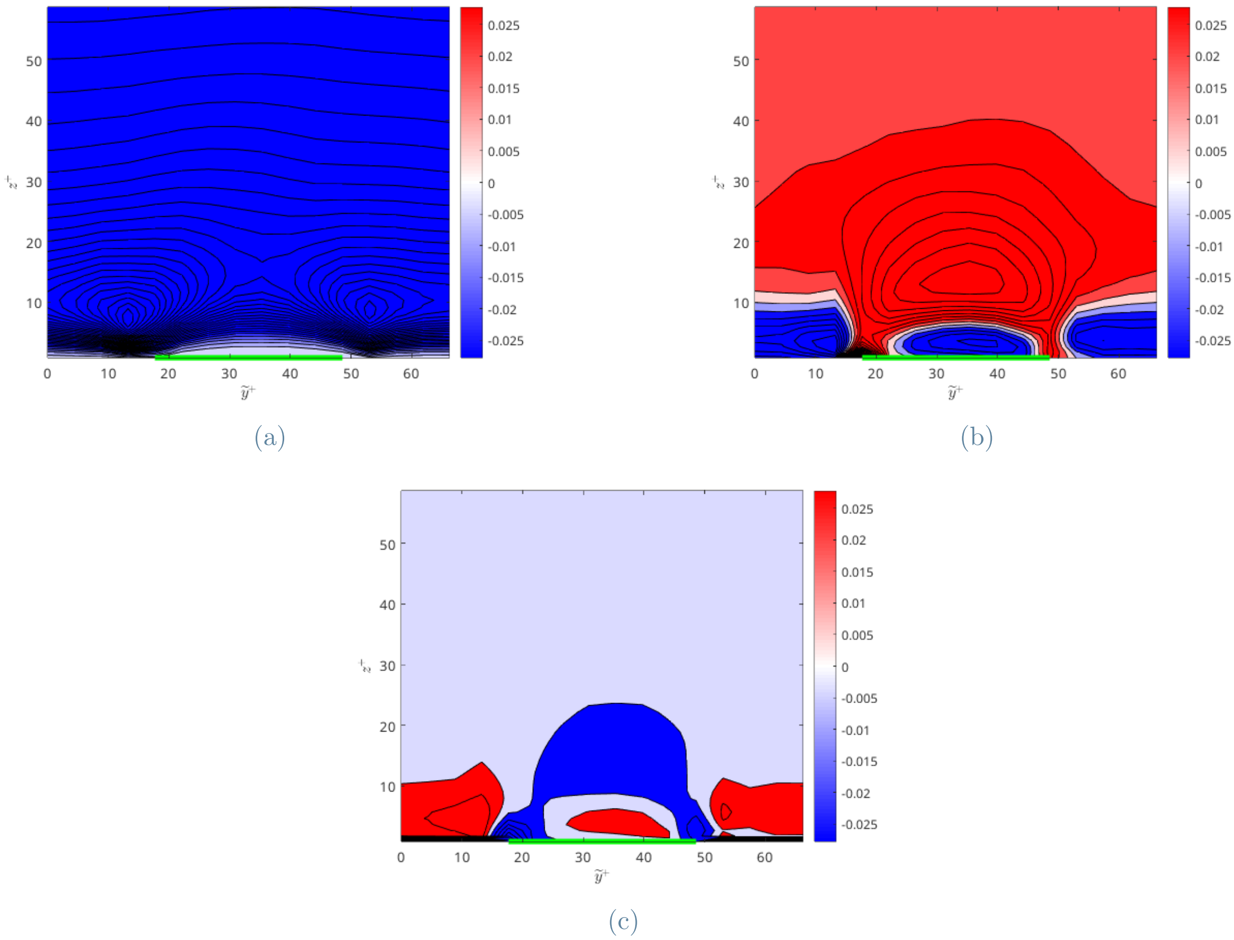

Figure 18: (a) P''_{13}, b) Π''_{13}, c) $T''_{13} + Pr''_{13} + D''_{13} + M''_{13}$. Green lines: no-slip stripe

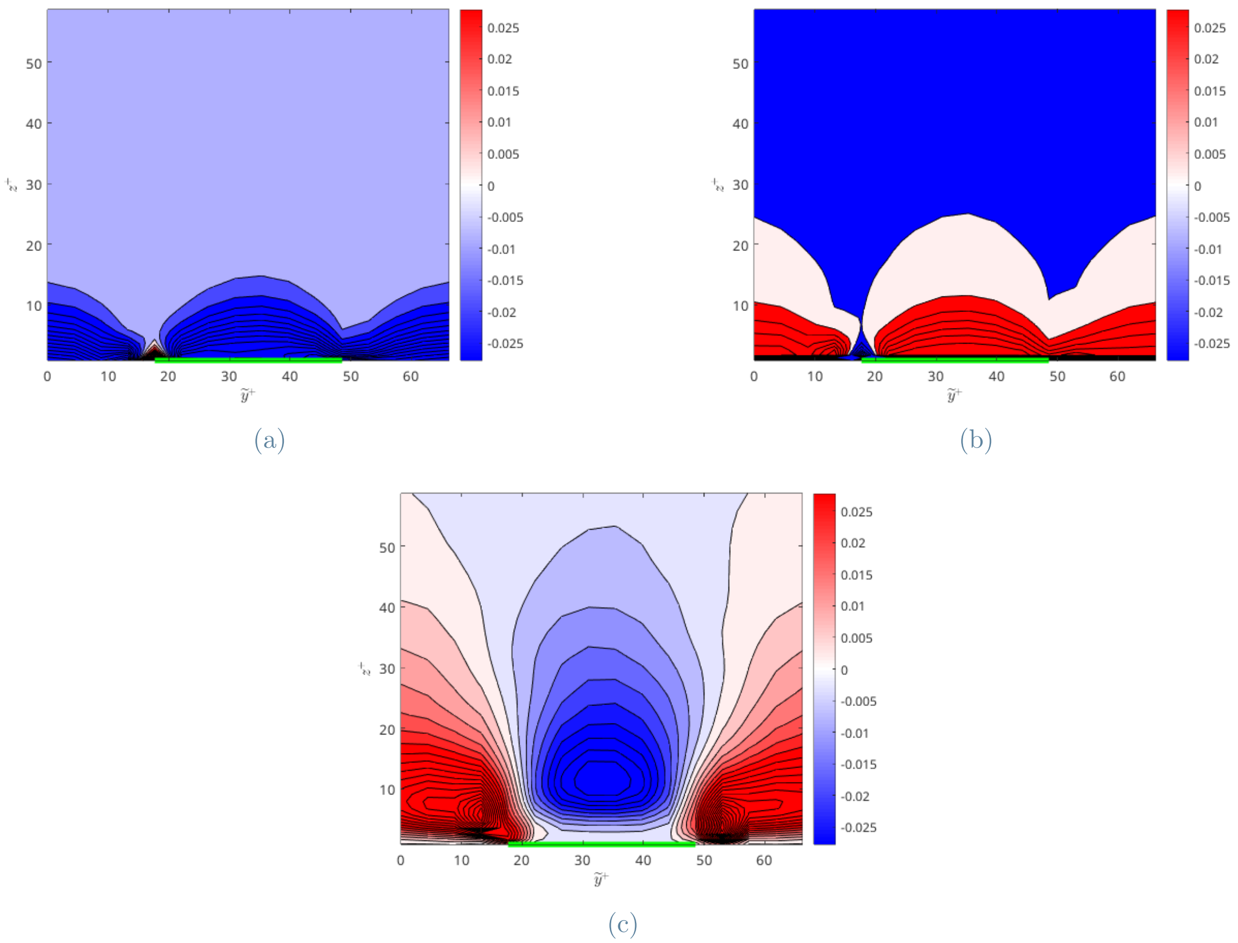

Figure 19: (a) $\widetilde{\Pi}_{13}$, b) $\widetilde{Pr}_{13}$, c) $P_{sc,13}$. Green lines: no-slip stripe

As mentioned before, the energy goes from the coherent field to the stochastic one, and successively to the coherent flow, so now the focus regards the budget equations for the stochastic field. From Figure 18, it can be noticed that P''_{13} is very high over the slip stripes, and also Π''_{13} is very intense in these regions. The effect of these two producing terms is partially balanced by the transport terms, which moves energy from the slip stripes to the region above the no-slip ones to redistribute the excess of -$\langle u''w''\rangle$. However, the action of the transport terms is not sufficient to close the balance over the slip stripes. In fact, looking briefly at Figure 19, it emerges that above the slip stripes $P_{sc,13}$ moves energy from the stochastic field to the coherent one, helping to drain the excessive shear stress -$\langle u''w''\rangle$ in these regions. Once that energy is moved to the coherent field, the high derivatives in the wall normal direction of this field generate high values of $\widetilde{\Pi}_{13}$ above the slip regions. Finally, the effect of $P_{sc,13}$ and $\widetilde{\Pi}_{13}$ is balanced by the pressure transport, which moves energy toward the bulk of the flow (Figure 19). Over the no-slip region, the evolution of both the coherent and stochastic shear stress is very similar compared to the reference case. In fact, for both fields the pressure strain term represents an intense source term, and its effect is countered by the pressure transport ([21]).

4. Conclusions

In this work, the effect of secondary motions induced by SH surfaces on near-wall turbulence has been investigated. In order to obtain the required results, the data from a DNS performed in a turbulent channel flow over SH surfaces have been post-processed through a centered-finite differences post processing code. First of all, the properties of the mean flow have been computed, and the main differences with respect to the reference case have been highlighted. Once the analysis of the mean flow has been concluded, the Reynolds stresses $\langle u'_i u'_j\rangle$ have been compared to those obtained in the reference case. The difference in wall shear stress has been related to a change in drag through the triple decomposed FIK identity. This relation has been used to separate the contributions to the change in drag of both the coherent and the stochastic field. Furthermore, the use of the FIK identity has enabled to compute the achieved percentage of drag reduction. Once the impact of coherent motions on the skin friction coefficient has been quantified, budget equations for Reynolds stresses have been used to investigate the evolution in space of the shear stress $\langle u'w' \rangle$. In particular, these equations have been analyzed to explain the increase in the wall shear stress observed at the wall. Once this objective has been achieved, in order to provide a better understanding of the formation of the coherent shear stress, the triple decomposition have been applied to the previous mentioned budget equations. Finally, since SH surfaces induce strong heterogeneities in the spanwise direction, the triple decomposed budget equations have been observed in two dimensions.

Looking at the logarithmic velocity profile of the mean streamwise velocity, it is observed that SH surfaces induce an upward displacement of the velocity profile obtained in the reference case. This displacement clearly shows the ability of SH surfaces to obtain drag reduction. However, in the logarithmic region, a reduction in the amount of drag reduction is observed. This phenomenon has been explained by looking at the wall shear stress $\langle u'w' \rangle$, which is higher compared to the reference case, and has a peak shifted toward the wall. Using the FIK identity and the triple decomposition, the increase in the coherent wall shear stress has been shown to have a negative effect on drag reduction. Despite this negative contribution, drag reduction is achieved using SH surfaces because the mean streamwise slip velocity at the wall greatly increases the value of U_b^+. To understand why the wall shear stress $\langle u'w' \rangle$ increases when SH surfaces are used, the budget equations for Reynolds stresses with Reynolds decomposition have been used. Using this tool, an increase in the Production of $-\langle u'w' \rangle$ is observed close to the wall. Furthermore, this increase has been related to an increase in the magnitude of $\langle w'w' \rangle$ near the wall. An explanation for the increase of this stress has been provided by looking at its budget equation, which highlights that $\langle w'w' \rangle$ is increased because Π_{33} (which is the main source term for this equation) is higher compared to the reference case. Taking into account these observations, the change in Π_{33} close to the wall has been related to the decrease in drag reduction observed in the logarithmic region. In order to provide more details about the increase in $-\langle u'w' \rangle$, the triple decomposed budget equations have been used. By looking at this equation, it emerges that the energy flow close to the wall involves energy moving from the mean flow to the fluctuating field, and successively, this energy moves toward the coherent field, causing a drag increase. Furthermore, the 2D budget equations equations highlight the fact that this energy transfer is predominant above the slip stripes, while the flow behavior above the no-slip stripes does not change so much with respect to the reference case.

Despite all the results obtained in this work, the physical mechanisms that move energy from the stochastic field to the coherent one represent an interesting object of investigation. Furthermore, it will be useful to increase the amount of drag reduction achievable through the use of super-hydrophobic surfaces. As said throughout this work, a disadvantage in the use of super-hydrophobic surfaces lies in the formation of coherent motions, which have a negative effect on drag reduction. For this reason, the investigation of mechanisms able to suppress the effect of coherent motions represents an interesting research activity that will enable to increase the use of SH surfaces in turbulent channel flows.

References

[1] N. Abderrahaman-Elena, C.T. Fairhall, and R. García-Mayoral. "Modulation of near-wall turbulence in the transitionally rough regime". In: *Journal of Fluid Mechanics* 865 (2019).

[2] N. Abderrahaman-Elena and R. García-Mayoral. "Geometry-induced fluctuations in the transitionally rough regime". In: *Journal of Physics* 708 (2016).

[3] D. Barros et al. "Bluff body drag manipulation using pulsed jets and Coanda effect". In: *Journal of Fluid Mechanics* 805 (2016).

[4] A. Busse and N.D. Sandham. "Influence of an anisotropic slip-length boundary condition on turbulent channel flow". In: *Physics of Fluids* 24 (2012).

[5] D. Chung, J.P. Monty, and N. Hutchins. "Similarity and structure of wall turbulence with lateral wall shear stress variations". In: *Journal of Fluid Mechanics* 847 (2018).

[6] S. Cipelli. "Efficient Direct Numerical Simulations of Straight and Sinusoidal Riblets in Turbulent Channel Flows". MA thesis. Politecnico di Milano, 2023.

[7] C.T. Fairhall, N. Abderrahaman-Elena, and R. García-Mayoral. "The effect of slip and surface texture on turbulence over superhydrophobic surfaces". In: *Journal of Fluid Mechanics* 861 (2019).

[8] K. Fukagata, K. Iwamoto, and N. Kasagi. “Contribution of Reynolds stresses distribution to the skin friction in wall-bounded flows”. In: *Physics of Fluids* 14 (2002).

[9] K. Fukagata, N. Kasagi, and P. Koumoutsakos. “A theoretical prediction of friction drag reduction in turbulent flow by superhydrophobic surfaces”. In: *Physics of Fluids* 18 (2006).

[10] K. Fukuda et al. “Frictional drag reduction with air lubrificant over a super-water-repellent surface”. In: *Journal of Marine Science and Techonology* 5 (2000).

[11] R. García-Mayoral, G. Gomez-De-Segura, and C.T. Fairhall. “The control of near-wall turbulence through surface texturing”. In: *Fluid Dynamics Research* 51 (2019).

[12] R. García-Mayoral and J. Jimenez. “Drag reduction by riblets”. In: *Physical Transactions of the Royal Society* 369 (2011).

[13] D. Goldstein, R. Handler, and L. Sirovich. “Direct numerical simulation of turbulent flow over a modelled riblet covered surface”. In: *Journal of Fluid Mechanics* 302 (1995).

[14] Y. Hasegawa, B. Frohnapfel, and N. Kasagi. “Effects of spatially varying slip length on friction drag reduction in wall-turbulence”. In: *Journal of Physics* 318 (2011).

[15] A.K.M.F. Hussain and W.C. Reynolds. “The mechanics of an organized wave in turbulent shear flow”. In: *Journal of Fluid Mechanics* 41 (1970).

[16] H. Hwang and J. Lee. “Secondary flows in turbulent boundary layers over longitudinal surface roughness”. In: *Physical Review Fluids* 3 (2018).

[17] J. Ibrahim et al. “The smooth-wall-like behaviour of turbulence over drag-altering surfaces: a unifying virtual-origin framework”. In: *Journal of Fluid Mechanics* 915 (2021).

[18] T. Kawata T Tsukahara. “Scale interactions in turbulent plane Couette flows in minimal domains”. In: *Journal of Fluid Mechanics* 911 (2021).

[19] P. Luchini. “Immersed-boundary simulation of turbulent flow past a sinusoidally undulated river bottom”. In: *European Journal of Mechanics-B/Fluids* 55 (2016).

[20] P. Luchini, F. Manzo, and A. Pozzi. “Resistance of a grooved surface to parallel flow and cross-flow”. In: *Journal of Fluid Mechanics* 228 (1991).

[21] N.N. Mansour, J. Kim, and P. Moin. “Reynolds-Stress and Dissipation Rate Budgets in a Turbulent Channel Flow”. In: *NASA Ames Researc Center* (1987).

[22] T. Min and J. Kim. “Effects of hydrophobic surface on skin-friction drag”. In: *Physics of Fluids* 16 (2004).

[23] D. Modesti, S. Endrikat, and D. Hutchins N. Chung. “Dispersive stresses in turbulent flow over riblets”. In: *Journal of Fluid Mechanics* 917 (2021).

[24] C.L.M.H. Navier. “Memoires sur le lois du mouvement des fluide”. In: *Memoires de l’Academie des sciences de l’Institut de France* 6 (1823).

[25] J. Neuhauser et al. “Simulation of turbulent flow over roughness strips”. In: *Journal of Fluid Mechanics* 945 (2022).

[26] S.B. Pope. *Turbulent Flows*. Cambridge University Press, 2000.

[27] L. Prandtl. “Einführung in die Grundbegriffe der Strömungslehre”. In: *Akademische Verlagsgesellschaft* (1931).

[28] M. Quadrio, P. Ricco, and C. Viotti. “Streamwise-traveling waves of spanwise wall velocity in a turbulent channel flow”. In: *Journal of Fluid Mechanics* 627 (2009).

[29] A. Rastegari and R. Akhavan. “On the mechanism of turbulent drag reduction with super-hydrophobic surfaces”. In: *Journal of Fluid Mechanics* 773 (2015).

[30] W. Reynolds and A. Hussain. “The mechanics of an organized wave in turbulent shear flow. part 3. theoretical models and comparisons with experiments”. In: *Journal of Fluid Mechanics* 54 (1972).

[31] J.P. Rothstein. “Slip on superhydrophobic surfaces”. In: *Annual Review of Fluid Mechanics* 42 (2010).

[32] J. Seo, R. García-Mayoral, and A. Mani. “Pressure fluctuations in turbulent flows over superhydrophobic surfaces”. In: *Center for Turbulence Research* (2013).

[33] J. Seo, R. García-Mayoral, and A. Mani. “Pressure fluctuations and interfacial robustness in turbulent flows over super-hydrophobic surfaces”. In: *Journal of Fluid Mechanics* 783 (2015).

[34] A. Stroh et al. “Rearrangement of secondary flow over spanwise heterogeneous roughness”. In: *Journal of Fluid Mechanics* 885 (2020).

[35] C. Xia et al. “Active flow control for bluff body drag reduction using reinforcement learning with partial measurements”. In: *Journal of Fluid Mechanics* 981 (2024).

[36] W. Xie, C.T. Fairhall, and R. García-Mayoral. “Resolving turbulence and drag over textured surfaces using texture-less simulations: the case of slip/no-slip textures”. In: *Journal of Fluid Mechanics* 1000 (2024).

A. Derivation of the budget equations for $\langle \widetilde{u}_i \widetilde{u}_j \rangle$ and $\langle u_i'' u_j'' \rangle$

Through the triple decomposition, the velocity field can be written as follows

$$u = U + \widetilde{u} + u'' \tag{28}$$

where U is the meanflow, $\widetilde{u}$ is the coherent field and u'' is the stochastic one. Furthermore, for a single component of the Reynolds stress tensor, the following equality holds

$$\langle u_i' u_j' \rangle = \langle \widetilde{u}_i \widetilde{u}_j \rangle + \langle u_i'' u_j'' \rangle \tag{29}$$

where the operator $\langle . \rangle$ performs an average in time, in the homogeneous direction x and on the number of texture periods. The above equality holds only if there is no correlation between the coherent and the stochastic fields, and the filter $\langle . \rangle$ fulfills this property.

A.1. Budget equations for U_i

Incompressible Navier–Stokes equations:

$$\frac{\partial u_i}{\partial t} + u_j \frac{\partial u_i}{\partial x_j} = -\frac{1}{\rho}\frac{\partial p}{\partial x_i} + \nu \frac{\partial^2 u_i}{\partial x_j \partial x_j} \tag{30}$$

Through the use of the triple decomposition:

$$\begin{aligned} &\frac{\partial}{\partial t}(U_i + \widetilde{u}_i + u_i'') + (U_j + \widetilde{u}_j + u_j'')\frac{\partial}{\partial x_j}(U_i + \widetilde{u}_i + u_i'') = \\ &-\frac{1}{\rho}\frac{\partial}{\partial x_i}(P + \widetilde{p} + p'') + \nu \frac{\partial^2}{\partial x_j \partial x_j}(U_i + \widetilde{u}_i + u_i'') \end{aligned} \tag{31}$$

It is expanded as

$$\begin{aligned} &\frac{\partial U_i}{\partial t} + \frac{\partial \widetilde{u}_i}{\partial t} + \frac{\partial u_i''}{\partial t} + U_j \frac{\partial U_i}{\partial x_j} + U_j \frac{\partial \widetilde{u}_i}{\partial x_j} + U_j \frac{\partial u_i''}{\partial x_j} + \widetilde{u}_j \frac{\partial U_i}{\partial x_j} + \widetilde{u}_j \frac{\partial \widetilde{u}_i}{\partial x_j} + \widetilde{u}_j \frac{\partial u_i''}{\partial x_j} \\ &+ u_j'' \frac{\partial U_i}{\partial x_j} + u_j'' \frac{\partial \widetilde{u}_i}{\partial x_j} + u_j'' \frac{\partial u_i''}{\partial x_j} = -\frac{1}{\rho}\frac{\partial P}{\partial x_i} - \frac{1}{\rho}\frac{\partial \widetilde{p}}{\partial x_i} - \frac{1}{\rho}\frac{\partial p''}{\partial x_i} \\ &+ \nu \frac{\partial^2 U_i}{\partial x_j \partial x_j} + \nu \frac{\partial^2 \widetilde{u}_i}{\partial x_j \partial x_j} + \nu \frac{\partial^2 u_i''}{\partial x_j \partial x_j} \end{aligned} \tag{32}$$

By applying the $\langle \cdot \rangle$ operator, which performs averaging in time and homogeneous directions, the budget equation for U_i is obtained:

$$\frac{\partial U_i}{\partial t} + U_j \frac{\partial U_i}{\partial x_j} + \left\langle \widetilde{u}_j \frac{\partial \widetilde{u}_i}{\partial x_j} \right\rangle + \left\langle \widetilde{u}_j \frac{\partial u_i''}{\partial x_j} \right\rangle + \left\langle u_j'' \frac{\partial \widetilde{u}_i}{\partial x_j} \right\rangle + \left\langle u_j'' \frac{\partial u_i''}{\partial x_j} \right\rangle = -\frac{1}{\rho}\frac{\partial P}{\partial x_i} + \nu \frac{\partial^2 U_i}{\partial x_j \partial x_j} \tag{33}$$

A.2. budget equations for $\langle \widetilde{u}_i \widetilde{u}_j \rangle$ and $\langle u_i'' u_j'' \rangle$

By using the $\langle . \rangle$ operator and the triple decomposition, budget equations for $\langle \widetilde{u}_i \widetilde{u}_j \rangle$ and $\langle u_i'' u_j'' \rangle$ can be derived starting from the Navier-Stokes equations written using Reynolds decomposition

$$\frac{\partial}{\partial t}(U_i + u_i') + (U_k + u_k') \frac{\partial}{\partial x_k}(U_i + u_i') = -\frac{1}{\rho} \frac{\partial}{\partial x_i}(P + p') + \nu \frac{\partial^2}{\partial x_k \partial x_k}(U_i + u_i') \tag{34}$$

Rearrange

$$\begin{aligned} &\frac{\partial}{\partial t}(U_i + u_i') + U_k \frac{\partial U_i}{\partial x_k} + U_k \frac{\partial u_i'}{\partial x_k} + u_k' \frac{\partial U_i}{\partial x_k} + u_k' \frac{\partial u_i'}{\partial x_k} \\ &= -\frac{1}{\rho} \frac{\partial}{\partial x_i}(P + p') + \nu \frac{\partial^2}{\partial x_k \partial x_k}(U_i + u_i') \end{aligned} \tag{35}$$

Multiply by u_j''

$$\begin{aligned} &u_j'' \frac{\partial U_i}{\partial t} + u_j'' \frac{\partial u_i'}{\partial t} + u_j'' U_k \frac{\partial U_i}{\partial x_k} + u_j'' U_k \frac{\partial u_i'}{\partial x_k} + u_j'' u_k' \frac{\partial U_i}{\partial x_k} + u_j'' u_k' \frac{\partial u_i'}{\partial x_k} \\ &= -\frac{1}{\rho} u_j'' \frac{\partial}{\partial x_i}(P + p') + \nu u_j'' \frac{\partial^2}{\partial x_k \partial x_k}(U_i + u_i') \end{aligned} \tag{36}$$

Replace i with j

$$\begin{aligned} &u_i'' \frac{\partial U_j}{\partial t} + u_i'' \frac{\partial u_j'}{\partial t} + u_i'' U_k \frac{\partial U_j}{\partial x_k} + u_i'' U_k \frac{\partial u_j'}{\partial x_k} + u_i'' u_k' \frac{\partial U_j}{\partial x_k} + u_i'' u_k' \frac{\partial u_j'}{\partial x_k} \\ &= -\frac{1}{\rho} u_i'' \frac{\partial}{\partial x_j}(P + p') + \nu u_i'' \frac{\partial^2}{\partial x_k \partial x_k}(U_j + u_j') \end{aligned} \tag{37}$$

Sum Equations 36 and 37

$$\begin{aligned} &u_j'' \frac{\partial U_i}{\partial t} + u_i'' \frac{\partial U_j}{\partial t} + u_j'' \frac{\partial u_i'}{\partial t} + u_i'' \frac{\partial u_j'}{\partial t} + u_j'' U_k \frac{\partial U_i}{\partial x_k} + u_i'' U_k \frac{\partial U_j}{\partial x_k} \\ &+ u_j'' U_k \frac{\partial u_i'}{\partial x_k} + u_i'' U_k \frac{\partial u_j'}{\partial x_k} + u_j'' u_k' \frac{\partial U_i}{\partial x_k} + u_i'' u_k' \frac{\partial U_j}{\partial x_k} + u_j'' u_k' \frac{\partial u_i'}{\partial x_k} + u_i'' u_k' \frac{\partial u_j'}{\partial x_k} \\ &= -\frac{1}{\rho} u_j'' \frac{\partial}{\partial x_i}(P + p') - \frac{1}{\rho} u_i'' \frac{\partial}{\partial x_j}(P + p') \\ &+ \nu u_j'' \frac{\partial^2}{\partial x_k \partial x_k}(U_i + u_i') + \nu u_i'' \frac{\partial^2}{\partial x_k \partial x_k}(U_j + u_j') \end{aligned} \tag{38}$$

Apply the $\langle . \rangle$ operator and recall Equation 33

$$\begin{aligned} &U_k \left\langle u_j'' \frac{\partial u_i'}{\partial x_k} \right\rangle + U_k \left\langle u_i'' \frac{\partial u_j'}{\partial x_k} \right\rangle + \langle u_j'' u_k' \rangle \frac{\partial U_i}{\partial x_k} + \langle u_i'' u_k' \rangle \frac{\partial U_j}{\partial x_k} + \left\langle u_j'' u_k' \frac{\partial u_i'}{\partial x_k} \right\rangle \\ &+ \left\langle u_i'' u_k' \frac{\partial u_j'}{\partial x_k} \right\rangle = -\frac{1}{\rho} \left\langle u_j'' \frac{\partial p'}{\partial x_i} \right\rangle - \frac{1}{\rho} \left\langle u_i'' \frac{\partial p'}{\partial x_j} \right\rangle \\ &+ \nu \left\langle u_j'' \frac{\partial^2 u_i'}{\partial x_k \partial x_k} \right\rangle + \nu \left\langle u_i'' \frac{\partial^2 u_j'}{\partial x_k \partial x_k} \right\rangle \end{aligned} \tag{39}$$

Recall that $u_i' = \widetilde{u}_i + u_i''$, $u_j' = \widetilde{u}_j + u_j''$ and $p' = \widetilde{p} + p''$

$$\begin{aligned} &U_k \left\langle u_j'' \frac{\partial}{\partial x_k}(\widetilde{u}_i + u_i'') \right\rangle + U_k \left\langle u_i'' \frac{\partial}{\partial x_k}(\widetilde{u}_j + u_j'') \right\rangle \\ &+ \langle u_j''(\widetilde{u}_k + u_k'') \rangle \frac{\partial}{\partial x_k} U_i + \langle u_i''(\widetilde{u}_k + u_k'') \rangle \frac{\partial}{\partial x_k} U_j \\ &+ \left\langle u_j''(\widetilde{u}_k + u_k'') \frac{\partial}{\partial x_k}(\widetilde{u}_i + u_i'') \right\rangle + \left\langle u_i''(\widetilde{u}_k + u_k'') \frac{\partial}{\partial x_k}(\widetilde{u}_j + u_j'') \right\rangle \\ &= -\frac{1}{\rho} \left\langle u_j'' \frac{\partial}{\partial x_i}(\widetilde{p} + p'') \right\rangle - \frac{1}{\rho} \left\langle u_i'' \frac{\partial}{\partial x_j}(\widetilde{p} + p'') \right\rangle \\ &+ \nu \left\langle u_j'' \frac{\partial^2}{\partial x_k \partial x_k}(\widetilde{u}_i + u_i'') \right\rangle + \nu \left\langle u_i'' \frac{\partial^2}{\partial x_k \partial x_k}(\widetilde{u}_j + u_j'') \right\rangle \end{aligned} \tag{40}$$

Considering that $\langle \widetilde{u}_i u''_j \rangle = 0$, $\langle u''_i \widetilde{u}_j = 0$ and $\langle u''_i \widetilde{p} \rangle = 0$

$$\begin{aligned}
&U_k \langle u''_j \frac{\partial u''_i}{\partial x_k} \rangle + U_k \langle u''_i \frac{\partial u''_j}{\partial x_k} \rangle + \langle u''_j u''_k \rangle \frac{\partial U_i}{\partial x_k} + \langle u''_i u''_k \rangle \frac{\partial U_j}{\partial x_k} + \langle u''_j \widetilde{u}_k \frac{\partial \widetilde{u}_i}{\partial x_k} \rangle + \\
&\langle u''_j u''_k \frac{\partial \widetilde{u}_i}{\partial x_k} \rangle + \langle u''_j \widetilde{u}_k \frac{\partial u''_i}{\partial x_k} \rangle + \langle u''_j u''_k \frac{\partial u''_i}{\partial x_k} \rangle + \langle u''_i \widetilde{u}_k \frac{\partial \widetilde{u}_j}{\partial x_k} \rangle + \langle u''_i u''_k \frac{\partial \widetilde{u}_j}{\partial x_k} \rangle + \\
&\langle u''_i \widetilde{u}_k \frac{\partial u''_j}{\partial x_k} \rangle + \langle u''_i u''_k \frac{\partial u''_j}{\partial x_k} \rangle = -\frac{1}{\rho} \langle u''_j \frac{\partial p''}{\partial x_i} \rangle - \frac{1}{\rho} \langle u''_i \frac{\partial p''}{\partial x_j} \rangle + \\
&\nu \langle u''_j \frac{\partial^2 u''_i}{\partial x_k \partial x_k} \rangle + \nu \langle u''_i \frac{\partial^2 u''_j}{\partial x_k \partial x_k} \rangle
\end{aligned} \tag{41}$$

By further manipulation

$$\begin{aligned}
&U_k \langle \frac{\partial}{\partial x_k} u''_i u''_j \rangle + \langle u''_j u''_k \rangle \frac{\partial U_i}{\partial x_k} + \langle u''_i u''_k \rangle \frac{\partial U_j}{\partial x_k} + \langle u''_j \widetilde{u}_k \frac{\partial \widetilde{u}_i}{\partial x_k} \rangle + \langle u''_j u''_k \frac{\partial \widetilde{u}_i}{\partial x_k} \rangle + \\
&\frac{\partial}{\partial x_k} \langle u''_j u''_i \widetilde{u}_k \rangle + \frac{\partial}{\partial x_k} \langle u''_j u''_i u''_k \rangle + \langle u''_i \widetilde{u}_k \frac{\partial \widetilde{u}_j}{\partial x_k} \rangle + \langle u''_i u''_k \frac{\partial \widetilde{u}_j}{\partial x_k} \rangle = -\frac{1}{\rho} \langle u''_j \frac{\partial p''}{\partial x_i} \rangle - \\
&\frac{1}{\rho} \langle u''_i \frac{\partial p''}{\partial x_j} \rangle + \nu \frac{\partial^2}{\partial x_k \partial x_k} \langle u''_i u''_j \rangle - 2\nu \langle \frac{\partial u''_i}{\partial x_k} \frac{\partial u''_j}{\partial x_k} \rangle
\end{aligned} \tag{42}$$

Performing one last manipulation

$$\begin{aligned}
&U_k \frac{\partial}{\partial x_k} \langle u''_i u''_j \rangle + \langle u''_j u''_k \rangle \frac{\partial U_i}{\partial x_k} + \langle u''_i u''_k \rangle \frac{\partial U_j}{\partial x_k} + \frac{\partial}{\partial x_k} \langle u''_j \widetilde{u}_k \widetilde{u}_i \rangle - \langle \widetilde{u}_i \widetilde{u}_k \frac{\partial u''_j}{\partial x_k} \rangle + \\
&\frac{\partial}{\partial x_k} \langle u''_j u''_k \widetilde{u}_i \rangle + \langle u''_j u''_k \frac{\partial \widetilde{u}_i}{\partial x_k} \rangle + \frac{\partial}{\partial x_k} \langle u''_i \widetilde{u}_j \widetilde{u}_k \rangle - \langle \widetilde{u}_j \widetilde{u}_k \frac{\partial u''_i}{\partial x_k} \rangle + \langle u''_i u''_k \frac{\partial \widetilde{u}_j}{\partial x_k} \rangle + \\
&\frac{\partial}{\partial x_k} \langle u''_j \widetilde{u}_k u''_i \rangle + \frac{\partial}{\partial x_k} \langle u''_j u''_k u''_i \rangle = -\frac{1}{\rho} \langle u''_j \frac{\partial p''}{\partial x_i} \rangle - \frac{1}{\rho} \langle u''_i \frac{\partial p''}{\partial x_j} \rangle + \\
&\nu \frac{\partial^2}{\partial x_k \partial x_k} \langle u''_i u''_j \rangle - 2\nu \langle \frac{\partial u''_i}{\partial x_k} \frac{\partial u''_j}{\partial x_k} \rangle
\end{aligned} \tag{43}$$

These equations represent the budget equations for $\langle u''_i u_j \rangle$. The budget equations for $\langle \widetilde{u}_i \widetilde{u}_j \rangle$ are obtained by multiplying Equation 35 by $\widetilde{u}_j$, and then the procedure is unchanged. In fact, the budget equations for $\langle \widetilde{u}_i \widetilde{u}_j \rangle$ are identical to 43, but the superscripts $\widetilde{.}$ and $.''$ are switched between each other.

B. Idempotency of the $\widetilde{.}$ operator

As mentioned in the previous section, Equation 29 is valid only if there is no correlation between the texture-induced field and the fluctuating one. This property is obtained only if the idempotency of the $\widetilde{.}$ filter is proved, which means that

$$\widetilde{\widetilde{u}} = \widetilde{u} \tag{44}$$

The proof is reported below

$$\begin{aligned}
\widetilde{\widetilde{u}} &= (\widetilde{u - U - u''}) \\
&= \widetilde{u} - \widetilde{U} - \widetilde{u''}
\end{aligned} \tag{45}$$

Recalling the definition of the $\widetilde{.}$ operator, $\widetilde{U} = 0$ can be prooved, while $\widetilde{u}'' = 0$ comes from the fact that u'' is a fluctuating field, and so its mean value is null by definition. In conclusion, Equation 45 has been reduced to 44, which prooves the requested idempotency.

C. Budget equations for $\langle \widetilde{u}_i \widetilde{u}_j \rangle$ and $\langle u''_i u''_j \rangle$ written fo every component of these stresses

Budget equation for $\langle \widetilde{u}\widetilde{u} \rangle$:

$$
\begin{aligned}
&V\frac{\partial}{\partial y}\langle\widetilde{u}\widetilde{u}\rangle+W\frac{\partial}{\partial z}\langle\widetilde{u}\widetilde{u}\rangle+2\langle\widetilde{u}\widetilde{w}\rangle\frac{\partial}{\partial z}U+\frac{\partial}{\partial y}\langle\widetilde{u}\widetilde{u}\widetilde{v}\rangle+\frac{\partial}{\partial z}\langle\widetilde{u}\widetilde{u}\widetilde{w}\rangle+\\
&\frac{\partial}{\partial y}\langle\widetilde{u}\widetilde{u}v''\rangle+\frac{\partial}{\partial z}\langle\widetilde{u}\widetilde{u}w''\rangle+\frac{\partial}{\partial y}\langle u''\widetilde{u}v''\rangle+\frac{\partial}{\partial z}\langle u''\widetilde{u}w''\rangle+\frac{\partial}{\partial y}\langle\widetilde{u}u''v''\rangle+\\
&\frac{\partial}{\partial z}\langle\widetilde{u}u''w''\rangle+2\left\langle\widetilde{u}\widetilde{u}\frac{\partial}{\partial x}u''\right\rangle+2\left\langle\widetilde{u}\widetilde{v}\frac{\partial}{\partial y}u''\right\rangle+2\left\langle\widetilde{u}\widetilde{w}\frac{\partial}{\partial z}u''\right\rangle-2\left\langle u''v''\frac{\partial}{\partial y}\widetilde{u}\right\rangle-\\
&2\left\langle u''w''\frac{\partial}{\partial z}\widetilde{u}\right\rangle=\nu\frac{\partial^2}{\partial z\partial z}\langle\widetilde{u}\widetilde{u}\rangle-2\nu\left\langle\frac{\partial}{\partial y}\widetilde{u}\frac{\partial}{\partial y}\widetilde{u}\right\rangle-2\nu\left\langle\frac{\partial}{\partial z}\widetilde{u}\frac{\partial}{\partial z}\widetilde{u}\right\rangle
\end{aligned}
\tag{46}
$$

Budget equation for $\langle\widetilde{v}\widetilde{v}\rangle$:

$$
\begin{aligned}
&V\frac{\partial}{\partial y}\langle\widetilde{v}\widetilde{v}\rangle+W\frac{\partial}{\partial z}\langle\widetilde{v}\widetilde{v}\rangle+2\langle\widetilde{v}\widetilde{w}\rangle\frac{\partial}{\partial z}V++\frac{\partial}{\partial y}\langle\widetilde{v}\widetilde{v}\widetilde{v}\rangle+\frac{\partial}{\partial z}\langle\widetilde{v}\widetilde{v}\widetilde{w}\rangle+\\
&\frac{\partial}{\partial y}\langle\widetilde{v}\widetilde{v}v''\rangle+\frac{\partial}{\partial z}\langle\widetilde{v}\widetilde{v}w''\rangle+\frac{\partial}{\partial y}\langle v''\widetilde{v}v''\rangle+\frac{\partial}{\partial z}\langle v''\widetilde{v}w''\rangle+\frac{\partial}{\partial y}\langle\widetilde{v}v''v''\rangle+\\
&\frac{\partial}{\partial z}\langle\widetilde{v}v''w''\rangle+2\left\langle\widetilde{v}\widetilde{u}\frac{\partial}{\partial x}v''\right\rangle+2\left\langle\widetilde{v}\widetilde{v}\frac{\partial}{\partial y}v''\right\rangle+2\left\langle\widetilde{v}\widetilde{w}\frac{\partial}{\partial z}v''\right\rangle-2\left\langle v''v''\frac{\partial}{\partial y}\widetilde{v}\right\rangle-\\
&2\left\langle v''w''\frac{\partial}{\partial z}\widetilde{v}\right\rangle=-\frac{2}{\rho}\frac{\partial}{\partial y}\langle\widetilde{p}\widetilde{v}\rangle+\frac{2}{\rho}\langle\widetilde{p}\frac{\partial\widetilde{v}}{\partial y}\rangle+\nu\frac{\partial^2}{\partial y\partial y}\langle\widetilde{v}\widetilde{v}\rangle+\\
&\nu\frac{\partial^2}{\partial z\partial z}\langle\widetilde{v}\widetilde{v}\rangle-2\nu\left\langle\frac{\partial}{\partial y}\widetilde{v}\frac{\partial}{\partial y}\widetilde{v}\right\rangle-2\nu\left\langle\frac{\partial}{\partial z}\widetilde{v}\frac{\partial}{\partial z}\widetilde{v}\right\rangle
\end{aligned}
\tag{47}
$$

Budget equation for $\langle\widetilde{w}\widetilde{w}\rangle$:

$$
\begin{aligned}
&V\frac{\partial}{\partial y}\langle\widetilde{w}\widetilde{w}\rangle+W\frac{\partial}{\partial z}\langle\widetilde{w}\widetilde{w}\rangle+2\langle\widetilde{w}\widetilde{w}\rangle\frac{\partial}{\partial z}W++\frac{\partial}{\partial y}\langle\widetilde{w}\widetilde{w}\widetilde{v}\rangle+\frac{\partial}{\partial z}\langle\widetilde{w}\widetilde{w}\widetilde{w}\rangle+\\
&\frac{\partial}{\partial y}\langle\widetilde{w}\widetilde{w}v''\rangle+\frac{\partial}{\partial z}\langle\widetilde{w}\widetilde{w}w''\rangle+\frac{\partial}{\partial y}\langle w''\widetilde{w}v''\rangle+\frac{\partial}{\partial z}\langle w''\widetilde{w}w''\rangle+\frac{\partial}{\partial y}\langle\widetilde{w}w''v''\rangle+\\
&\frac{\partial}{\partial z}\langle\widetilde{w}w''w''\rangle+2\left\langle\widetilde{w}\widetilde{u}\frac{\partial}{\partial x}w''\right\rangle+2\left\langle\widetilde{w}\widetilde{v}\frac{\partial}{\partial y}w''\right\rangle+2\left\langle\widetilde{w}\widetilde{w}\frac{\partial}{\partial z}w''\right\rangle-2\left\langle w''v''\frac{\partial}{\partial y}\widetilde{w}\right\rangle-\\
&2\left\langle w''w''\frac{\partial}{\partial z}\widetilde{w}\right\rangle=-\frac{2}{\rho}\frac{\partial}{\partial z}\langle\widetilde{p}\widetilde{w}\rangle+\frac{2}{\rho}\langle\widetilde{p}\frac{\partial\widetilde{w}}{\partial z}\rangle+\nu\frac{\partial^2}{\partial y\partial y}\langle\widetilde{w}\widetilde{w}\rangle+\\
&\nu\frac{\partial^2}{\partial z\partial z}\langle\widetilde{w}\widetilde{w}\rangle-2\nu\left\langle\frac{\partial}{\partial y}\widetilde{w}\frac{\partial}{\partial y}\widetilde{w}\right\rangle-2\nu\left\langle\frac{\partial}{\partial z}\widetilde{w}\frac{\partial}{\partial z}\widetilde{w}\right\rangle
\end{aligned}
\tag{48}
$$

Budget equation for $\langle\widetilde{u}\widetilde{w}\rangle$:

$$
\begin{aligned}
&V\frac{\partial}{\partial y}\langle\widetilde{u}\widetilde{w}\rangle+W\frac{\partial}{\partial z}\langle\widetilde{u}\widetilde{w}\rangle+\langle\widetilde{u}\widetilde{w}\rangle\frac{\partial}{\partial z}W+\langle\widetilde{w}\widetilde{w}\rangle\frac{\partial}{\partial z}U+\frac{\partial}{\partial y}\langle\widetilde{u}\widetilde{w}\widetilde{v}\rangle+\frac{\partial}{\partial z}\langle\widetilde{u}\widetilde{w}\widetilde{w}\rangle+\\
&\frac{\partial}{\partial y}\langle\widetilde{u}\widetilde{w}v''\rangle+\frac{\partial}{\partial z}\langle\widetilde{u}\widetilde{w}w''\rangle+\frac{\partial}{\partial y}\langle u''\widetilde{w}v''\rangle+\frac{\partial}{\partial z}\langle u''\widetilde{w}w''\rangle+\frac{\partial}{\partial y}\langle\widetilde{u}w''v''\rangle+\\
&\frac{\partial}{\partial z}\langle\widetilde{u}w''w''\rangle+\left\langle\widetilde{w}\widetilde{u}\frac{\partial}{\partial x}u''\right\rangle+\left\langle\widetilde{w}\widetilde{v}\frac{\partial}{\partial y}u''\right\rangle+\left\langle\widetilde{w}\widetilde{w}\frac{\partial}{\partial z}u''\right\rangle-\left\langle u''v''\frac{\partial}{\partial y}\widetilde{w}\right\rangle-\\
&\left\langle u''w''\frac{\partial}{\partial z}\widetilde{w}\right\rangle+\left\langle\widetilde{u}\widetilde{u}\frac{\partial}{\partial x}w''\right\rangle+\left\langle\widetilde{u}\widetilde{v}\frac{\partial}{\partial y}w''\right\rangle+\left\langle\widetilde{u}\widetilde{w}\frac{\partial}{\partial z}w''\right\rangle-\left\langle w''v''\frac{\partial}{\partial y}\widetilde{u}\right\rangle-\left\langle w''w''\frac{\partial}{\partial z}\widetilde{u}\right\rangle=\\
&-\frac{1}{\rho}\frac{\partial}{\partial z}\langle\widetilde{p}\widetilde{u}\rangle+\frac{1}{\rho}\langle\widetilde{p}\frac{\partial\widetilde{u}}{\partial z}\rangle+\nu\frac{\partial^2}{\partial y\partial y}\langle\widetilde{u}\widetilde{w}\rangle+\nu\frac{\partial^2}{\partial z\partial z}\langle\widetilde{u}\widetilde{w}\rangle-2\nu\left\langle\frac{\partial}{\partial y}\widetilde{u}\frac{\partial}{\partial y}\widetilde{w}\right\rangle-2\nu\left\langle\frac{\partial}{\partial z}\widetilde{u}\frac{\partial}{\partial z}\widetilde{w}\right\rangle
\end{aligned}
\tag{49}
$$

Budget equation for $\langle u''u''\rangle$:

$$
\begin{aligned}
&V\frac{\partial}{\partial y}\langle u''u''\rangle+W\frac{\partial}{\partial z}\langle u''u''\rangle+2\langle u''w''\rangle\frac{\partial}{\partial z}U+\frac{\partial}{\partial y}\langle u''u''v''\rangle+\frac{\partial}{\partial z}\langle u''u''w''\rangle+\\
&\frac{\partial}{\partial y}\langle u''u''\widetilde{v}\rangle+\frac{\partial}{\partial z}\langle u''u''\widetilde{w}\rangle+\frac{\partial}{\partial y}\langle\widetilde{u}u''\widetilde{v}\rangle+\frac{\partial}{\partial z}\langle\widetilde{u}u''\widetilde{w}\rangle+\frac{\partial}{\partial y}\langle u''\widetilde{u}\widetilde{v}\rangle+\\
&\frac{\partial}{\partial z}\langle u''\widetilde{u}\widetilde{w}\rangle-2\left\langle\widetilde{u}\widetilde{u}\frac{\partial}{\partial x}u''\right\rangle-2\left\langle\widetilde{u}\widetilde{v}\frac{\partial}{\partial y}u''\right\rangle-2\left\langle\widetilde{u}\widetilde{w}\frac{\partial}{\partial z}u''\right\rangle+2\left\langle u''v''\frac{\partial}{\partial y}\widetilde{u}\right\rangle+\\
&2\left\langle u''w''\frac{\partial}{\partial z}\widetilde{u}\right\rangle=\frac{2}{\rho}\langle p''\frac{\partial u''}{\partial x}\rangle+\nu\frac{\partial^2}{\partial y\partial y}\langle u''u''\rangle+\\
&\nu\frac{\partial^2}{\partial z\partial z}\langle u''u''\rangle-2\nu\left\langle\frac{\partial}{\partial y}u''\frac{\partial}{\partial y}u''\right\rangle-2\nu\left\langle\frac{\partial}{\partial z}u''\frac{\partial}{\partial z}u''\right\rangle
\end{aligned}
\tag{50}
$$

Budget equation for $\langle v''v''\rangle$:

$$
\begin{aligned}
&V\frac{\partial}{\partial y}\langle v''v''\rangle+W\frac{\partial}{\partial z}\langle v''v''\rangle+2\langle v''w''\rangle\frac{\partial}{\partial z}V++\frac{\partial}{\partial y}\langle v''v''v''\rangle+\frac{\partial}{\partial z}\langle v''v''w''\rangle+\\
&\frac{\partial}{\partial y}\langle v''v''\widetilde{v}\rangle+\frac{\partial}{\partial z}\langle v''v''\widetilde{w}\rangle+\frac{\partial}{\partial y}\langle\widetilde{v}v''\widetilde{v}\rangle+\frac{\partial}{\partial z}\langle\widetilde{v}v''\widetilde{w}\rangle+\frac{\partial}{\partial y}\langle v''\widetilde{v}\widetilde{v}\rangle+\\
&\frac{\partial}{\partial z}\langle v''\widetilde{v}\widetilde{w}\rangle-2\left\langle\widetilde{v}\widetilde{u}\frac{\partial}{\partial x}v''\right\rangle-2\left\langle\widetilde{v}\widetilde{v}\frac{\partial}{\partial y}v''\right\rangle-2\left\langle\widetilde{v}\widetilde{w}\frac{\partial}{\partial z}v''\right\rangle+2\left\langle v''v''\frac{\partial}{\partial y}\widetilde{v}\right\rangle+\\
&2\left\langle v''w''\frac{\partial}{\partial z}\widetilde{v}\right\rangle=-\frac{2}{\rho}\frac{\partial}{\partial y}\langle p''v''\rangle+\frac{2}{\rho}\langle p''\frac{\partial v''}{\partial y}\rangle+\nu\frac{\partial^2}{\partial y\partial y}\langle v''v''\rangle+\\
&\nu\frac{\partial^2}{\partial z\partial z}\langle v''v''\rangle-2\nu\left\langle\frac{\partial}{\partial y}v''\frac{\partial}{\partial y}v''\right\rangle-2\nu\left\langle\frac{\partial}{\partial z}v''\frac{\partial}{\partial z}v''\right\rangle
\end{aligned}
\tag{51}
$$

Budget equation for $\langle w''w''\rangle$:

$$
\begin{aligned}
&V\frac{\partial}{\partial y}\langle w''w''\rangle+W\frac{\partial}{\partial z}\langle w''w''\rangle+2\langle w''w''\rangle\frac{\partial}{\partial z}W++\frac{\partial}{\partial y}\langle w''w''v''\rangle+\frac{\partial}{\partial z}\langle w''w''w''\rangle+\\
&\frac{\partial}{\partial y}\langle w''w''\widetilde{v}\rangle+\frac{\partial}{\partial z}\langle w''w''\widetilde{w}\rangle+\frac{\partial}{\partial y}\langle\widetilde{w}w''\widetilde{v}\rangle+\frac{\partial}{\partial z}\langle\widetilde{w}w''\widetilde{w}\rangle+\frac{\partial}{\partial y}\langle w''\widetilde{w}\widetilde{v}\rangle+\\
&\frac{\partial}{\partial z}\langle w''\widetilde{w}\widetilde{w}\rangle-2\left\langle\widetilde{w}\widetilde{u}\frac{\partial}{\partial x}w''\right\rangle-2\left\langle\widetilde{w}\widetilde{v}\frac{\partial}{\partial y}w''\right\rangle-2\left\langle\widetilde{w}\widetilde{w}\frac{\partial}{\partial z}w''\right\rangle+2\left\langle w''v''\frac{\partial}{\partial y}\widetilde{w}\right\rangle+\\
&2\left\langle w''w''\frac{\partial}{\partial z}\widetilde{w}\right\rangle=-\frac{2}{\rho}\frac{\partial}{\partial z}\langle p''w''\rangle+\frac{2}{\rho}\langle p''\frac{\partial w''}{\partial z}\rangle+\nu\frac{\partial^2}{\partial y\partial y}\langle w''w''\rangle+\\
&\nu\frac{\partial^2}{\partial z\partial z}\langle w''w''\rangle-2\nu\left\langle\frac{\partial}{\partial y}w''\frac{\partial}{\partial y}w''\right\rangle-2\nu\left\langle\frac{\partial}{\partial z}w''\frac{\partial}{\partial z}w''\right\rangle
\end{aligned}
\tag{52}
$$

Budget equation for $\langle u''w''\rangle$:

$$
\begin{gathered}
V\frac{\partial}{\partial y}\left\langle u''w''\right\rangle + W\frac{\partial}{\partial z}\left\langle u''w''\right\rangle + \left\langle u''w''\right\rangle\frac{\partial}{\partial z}W + \left\langle w''w''\right\rangle\frac{\partial}{\partial z}U + \frac{\partial}{\partial y}\left\langle u''w''v''\right\rangle + \frac{\partial}{\partial z}\left\langle u''w''w''\right\rangle + \\
\frac{\partial}{\partial y}\left\langle u''w''\widetilde{v}\right\rangle + \frac{\partial}{\partial z}\left\langle u''w''\widetilde{w}\right\rangle + \frac{\partial}{\partial y}\left\langle \widetilde{u}w''\widetilde{v}\right\rangle + \frac{\partial}{\partial z}\left\langle \widetilde{u}w''\widetilde{w}\right\rangle + \frac{\partial}{\partial y}\left\langle u''\widetilde{w}\widetilde{v}\right\rangle + \\
\frac{\partial}{\partial z}\left\langle u''\widetilde{w}\widetilde{w}\right\rangle - \left\langle \widetilde{w}\widetilde{u}\frac{\partial}{\partial x}u''\right\rangle - \left\langle \widetilde{w}\widetilde{v}\frac{\partial}{\partial y}u''\right\rangle - \left\langle \widetilde{w}\widetilde{w}\frac{\partial}{\partial z}u''\right\rangle + \left\langle u''v''\frac{\partial}{\partial y}\widetilde{w}\right\rangle + \\
\left\langle u''w''\frac{\partial}{\partial z}\widetilde{w}\right\rangle - \left\langle \widetilde{u}\widetilde{u}\frac{\partial}{\partial x}w''\right\rangle - \left\langle \widetilde{u}\widetilde{v}\frac{\partial}{\partial y}w''\right\rangle - \left\langle \widetilde{u}\widetilde{w}\frac{\partial}{\partial z}w''\right\rangle + \left\langle w''v''\frac{\partial}{\partial y}\widetilde{u}\right\rangle + \left\langle w''w''\frac{\partial}{\partial z}\widetilde{u}\right\rangle = \\
-\frac{1}{\rho}\frac{\partial}{\partial z}\left\langle p''u''\right\rangle + \frac{1}{\rho}\left\langle p''\left(\frac{\partial u''}{\partial z} + \frac{\partial w''}{\partial x}\right)\right\rangle + \nu\frac{\partial^2}{\partial y\partial y}\left\langle u''w''\right\rangle + \\
\nu\frac{\partial^2}{\partial z\partial z}\left\langle u''w''\right\rangle - 2\nu\left\langle \frac{\partial}{\partial y}u''\frac{\partial}{\partial y}w''\right\rangle - 2\nu\left\langle \frac{\partial}{\partial z}u''\frac{\partial}{\partial z}w''\right\rangle
\end{gathered} \tag{53}
$$

D. Graphs of the terms involved in the Budget equations for $\langle \widetilde{u}_i\widetilde{u}_j\rangle$ and $\langle u_i''u_j''\rangle$

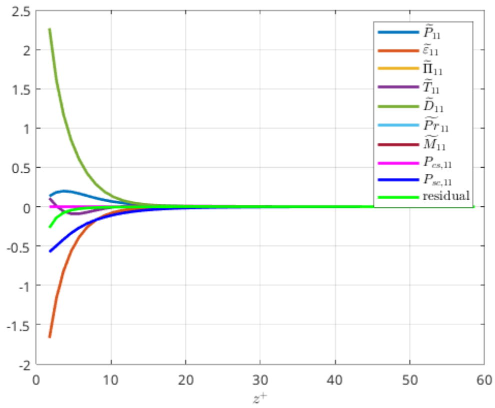

(a) $\langle \widetilde{u}\widetilde{u}\rangle$

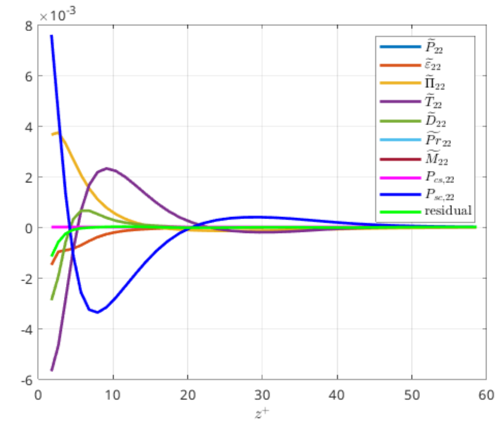

(b) $\langle \widetilde{v}\widetilde{v}\rangle$

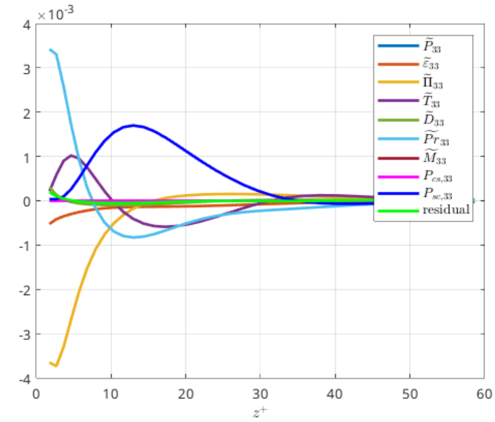

(c) $\langle \widetilde{w}\widetilde{w}\rangle$

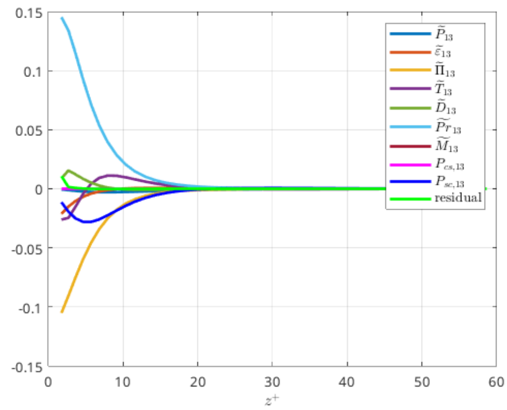

(d) $\langle \widetilde{u}\widetilde{w}\rangle$

Figure 20: Contributions to the budget equations for $\langle \widetilde{u}_i\widetilde{u}_j\rangle$

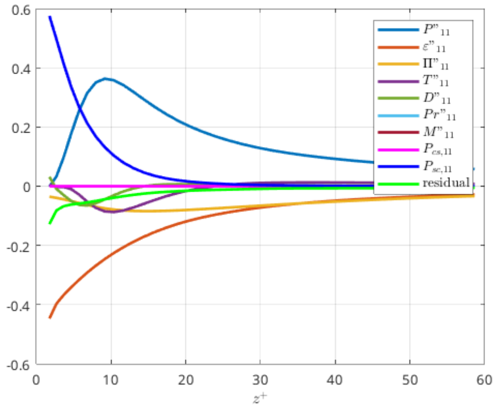

(a) $\langle u''u''\rangle$

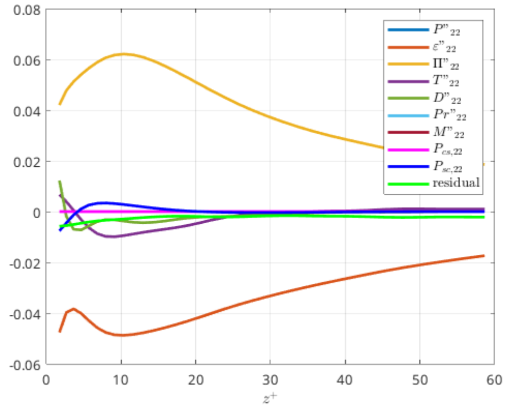

(b) $\langle v''v''\rangle$

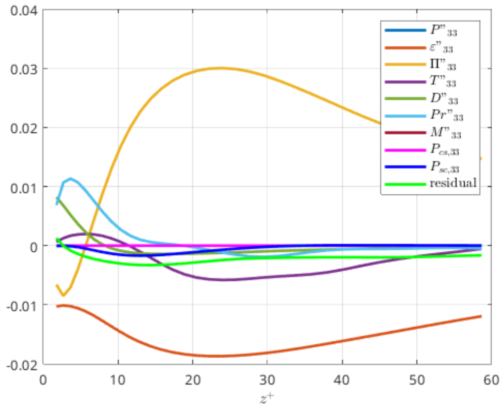

(c) $\langle w''w''\rangle$

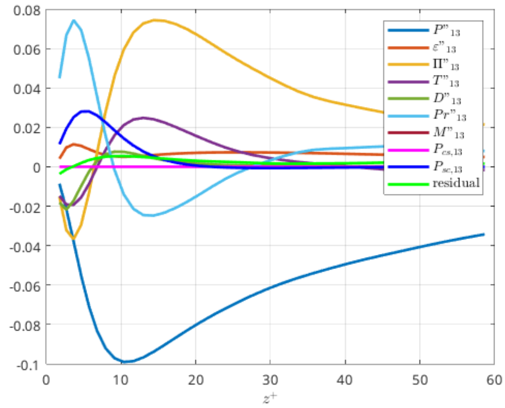

(d) $\langle u''w''\rangle$

Figure 21: Contributions to the budget equations for $\langle u_i''u_j''\rangle$

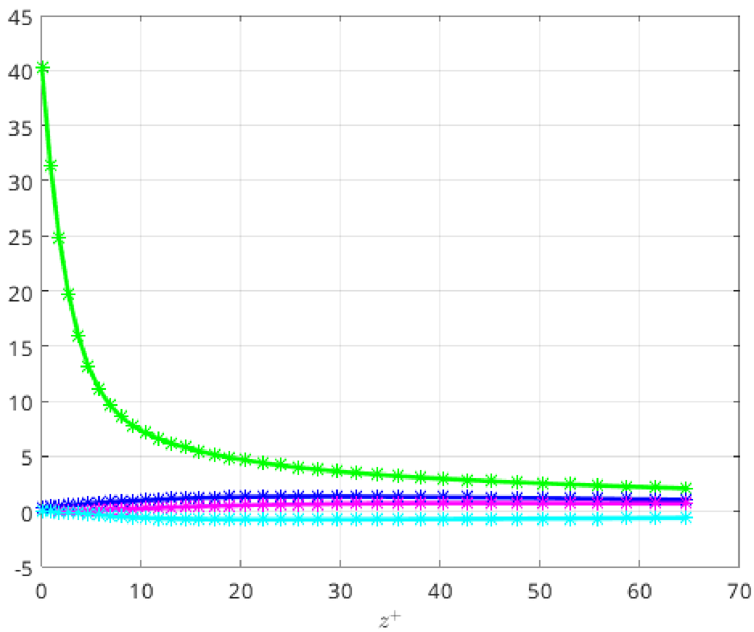

Figure 22: Solid lines: $\langle u_i'u_j'\rangle$; Dotted lines: $\langle \widetilde{u}_i\widetilde{u}_j\rangle + \langle u_i''u_j''\rangle$. Green: $\langle uu\rangle$, Blue: $\langle vv\rangle$, Purple: $\langle ww\rangle$, Cyan:$\langle uw\rangle$

Abstract in lingua italiana

I dati provenienti da una DNS condotta in un canale turbolento con superfici super-idrofobe sono stati trattati ed elaborati, in maniera tale da comprendere gli effetti introdotti da queste superfici sul coefficiente di attrito. La superficie idrofoba utilizzata all'interno di questo lavoro è composta da un alternarsi ,nella direzione dello span del canale, di strisce slip e no-slip, allineate con la direzione del flusso indisturbato. Le superfici idrofobe sono in grado di generare grandi riduzioni di attrito perché permettono al fluido che si muove sopra di esse di muoversi lungo la direzione longitudinale e lungo quella dello span del canale. In più, la presenza di un ordine nella struttura di queste superfici induce la formazione di un campo di moto coerente, il quale influenza la turboenza a parete. In particolare si è osservato che, nonostante si ottenga una diminuzione del coefficiente di attrito, il campo coerente induce un aumento dell'attività turbolenta a parete, la quale ha un effetto negativo sulla massima diminuzione di resistenza ottenibile. Questo campo coerente è stato separato da quello stocastico per mezzo di una tripla decomposizione dei campi di velocità e pressione. Successivamente, l'identità FIK è stata utilizzata per quantificare l'effetto negativo indotto dal campo coerente. Inoltre, le equazioni di bilancio per gli sforzi di Reynolds sono state utilizzate per capire cosa determina un'incremento della turbolenza vicino a parete. Infine, utilizzando le medesime equazioni di bilancio insieme alla tripla decomposizione, è stato possibile osservare come l'energia si trasmette dal campo coerente a quello stocastico e viceversa. Utilizzando tutti gli strumenti riportati, si è scoperto che la presenza di un campo coerente vicino a parete impatta negativamente la diminuzione massima di attrito ottenibile tramite un incremento dello sforzo di taglio vicino a parete. Inoltre, si è scoperto che questo effetto negativo è indotto da un flusso di energia a parete che va dal campo coerente verso quello stocastico.

Parole chiave: coefficiente di attrito, decomposizione tripla, superfici super-idrofobe